UNIVERSIDAD DE ANTIOQUIA

INSTITUTO DE FÍSICA
FACULTAD DE CIENCIAS EXACTAS Y NATURALES

M A S T E R T H E S I S

to obtain the title of

Master in Physics

Presented by

David Noreña

On The Formation Of Globular Clusters From Tidal Streams

Thesis Advisor: Juan Carlos Muñoz-Cuartas

prepared at Grupo de Física y Astrofísica Computacional, FACom

Acknowledgments

There several fundamental persons that contribute in one way or another to the development of this work.
First of all, I must to say that the tenacity, persistence and patience of my advisor, Juan Carlos Munoz-Cuartas, were the motors of this project. I was always grateful for keeping me forward even when I seem to falter.
I want to give my special thanks to Luis Fernando Quiroga-Pelaez for his constant support in the countless difficulties that emerged in the journey.
I must also make a special mention to those partners and friends whose presence helped me to hold myself.
Finally, I express my infinite gratitude to my parents, to whom I owe what I am and what I will be.

Contents

1 Introduction **1**

2 Theoretical Framework **7**
2.1 Globular Clusters . . . 7
2.1.1 Observations . . . 8
2.1.2 Formation . . . 11
2.1.3 Internal Dynamics . . . 13
2.1.4 External Dynamics . . . 16
2.2 Formation Scenarios of Metal-Rich Globular Clusters . 18
2.2.1 Globular Cluster from Galaxy Interactions . . . 18
2.2.2 Globular Cluster from Minor Mergers . . . 18
2.2.3 Globular Cluster from Super Star Formation Clumps 19
2.2.4 Globular Cluster from Turbulent Molecular Clouds . . . 19
2.3 Tidal Streams . . . 20
2.3.1 Observations . . . 20
2.3.2 Formation and Evolution . . . 20
2.4 Simulations . . . 21
2.4.1 *N*-Body Simulations . . . 21

3 Numerical Procedures **23**
3.1 Realization of the isolated galaxies . . . 23
3.1.1 The Host Galaxy . . . 23
3.1.2 The Satellite Galaxy . . . 25
3.2 Numerical Realizations . . . 28
3.3 Initial Positions . . . 29
3.4 Gravitational Potential Evaluation . . . 32
3.5 Density Computation . . . 33

4 Streams, Clusters and Substructures of the Satellite Galaxies **39**
4.1 Simulations without Gas . . . 39
4.1.1 Identification Of Streams . . . 40
4.1.2 Stream Substructures . . . 44
4.2 Simulations with Gas . . . 47
4.2.1 SPH Artificial Fragmentation . . . 48
4.2.2 Globular Clusters Candidates . . . 49
4.2.3 Analysis and Conclusions . . . 52

5 General Conclusions **61**

Bibliography 63

List of Figures

1.1 Globular and Open Clusters 1
1.2 Metallicity histogram for the GCs in the MW. 2
1.3 Location of the subpopulations in galactic-polar coordinates 3
1.4 Age *vs* Metallicity 4
1.5 Observed tidal streams 5

2.1 Color-Magnitude Diagram of M15 8

3.1 Numerical realization of a dark matter halo 25
3.2 Numerical realization of a galactic disc 26
3.3 Numerical realization of a galactic disc 27
3.4 Numerical realization of spheroidal satellite galaxy 29
3.5 Orbital circularity distribution 30
3.6 Pericentre distribution 32
3.7 Schematic representation of the initial configuration for each simulation 34
3.8 Gravitational potential projection in the radial direction 35
3.9 Density projection in the radial coordinate 36

4.1 Satellite center of mass distance to the galactic center as a function of time 42
4.2 Stream Identification 43
4.3 Mass gain/lose by a stream/satellite for different initial configurations 44
4.4 Potential map of the real and phase spaces 45
4.5 Potantial map of the real and phase spaces 46
4.6 Potential map of the real and phase spaces 50
4.7 Density of the particles in HR2 simulation. 51
4.8 Potential map of the real and phase spaces 52
4.9 Candidates in the three collisional simulation 53
4.10 Orbital evolution of the candidates 55
4.11 Dynamical evolution of clusters candidates 56
4.12 Thermodynamic state variables for the gas content in the candidates 57
4.13 Evolution of mass for each candidate 58

List of Tables

3.1 Fit parameters for the distributions of orbital parameters 30
3.2 Orbital configuration of the satellites 31

4.1 First experiment resolution values without gas 40
4.2 Second experiment resolution values without gas 40
4.3 First collisional experiment masses and particle numbers 47
4.4 Second collisional experiment masses and particle numbers 48
4.5 Third collisional experiment masses and particle numbers 49

Chapter 1

Introduction

Globular Clusters are old acquaintances for Astrophysics, but the interest in them remains unchanged. It has been established that a *globular cluster* is a stellar system consisting of between 10^4 to 10^6 gravitationally bound stars, spherically distributed around the center of mass of the cluster (see Figure 1.1). The number of belonging stars and spatial distribution are precisely two of the parameters that differentiate globular from *open clusters*, which are less numerous and their stars are distributed in less-defined shapes in space [Binney 2008]. In addition, for the Milky Way (MW), open clusters are found only in the galactic disk, unlike the vast distribution of globular clusters present both in the vicinity of the disc and all over the galactic halo [Carroll 2007]. With regard to this spatial distribution, globular clusters are divided in two distinct populations, being the metallicity and the ages of the clusters the main two features that differentiate them. Usually expressed in terms of the [Fe/H] abundance, the metallicity of a globular cluster around -0.5 places that cluster within the metal-rich clusters (MRGC) and clusters with values below -1 are the metal-poor ones (MPGC) [Harris 1999].

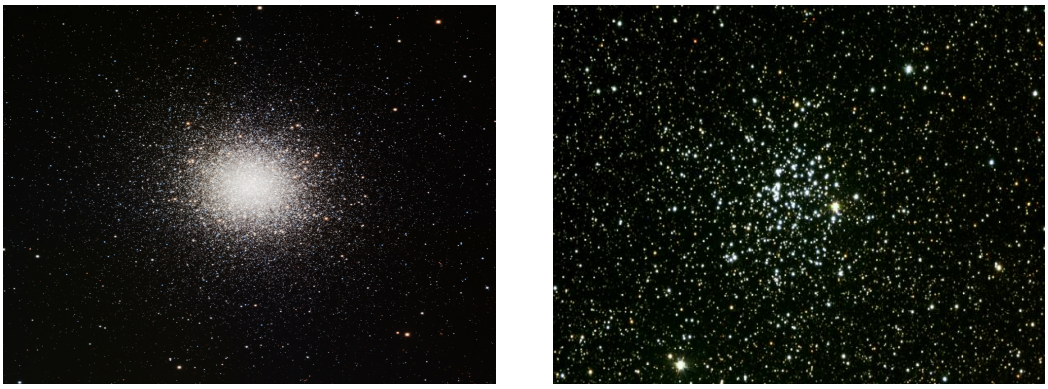

(a) Globular Cluster M13 (b) Open Cluster M52

Figure 1.1: (a) M13 is a 50 light-years in diameter globular cluster enclosing around 10^5 stars. Image Credit: T.A. Rector (University of Alaska Anchorage) and H. Schweiker (WIYN and NOAO/AURA/NSF). (b) M52 is an open cluster located 7000 light-years away from the Sun in the constellation of Cassiopeia. Image Credit: NOAO/AURA/NSF

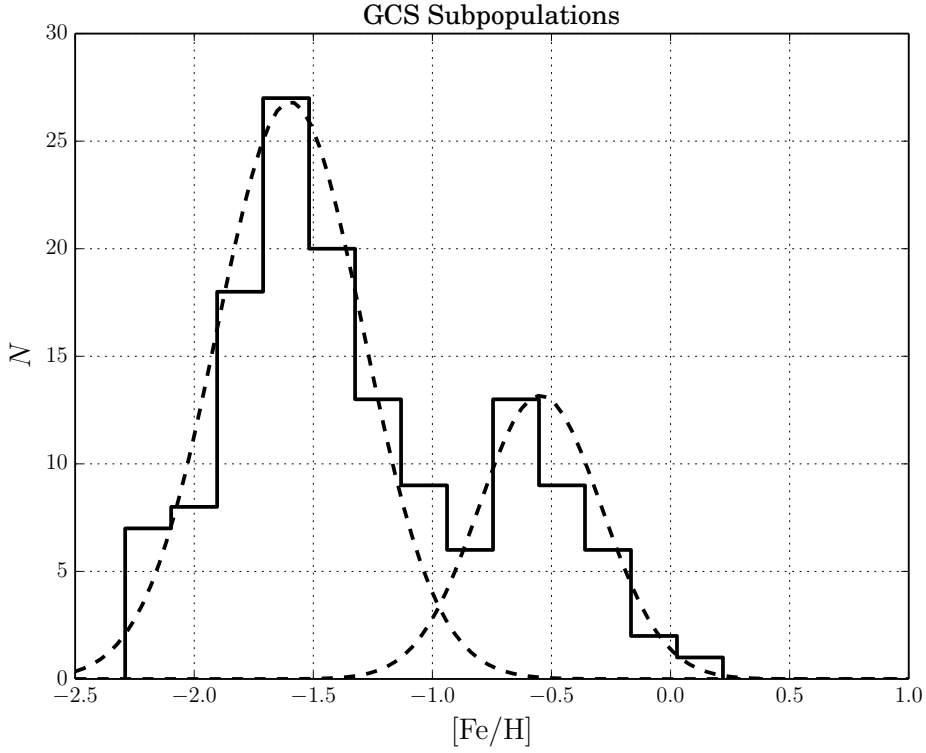

Figure 1.2: Metallicity distribution function for the globular clusters in the Milky Way. The metal poor clusters are more abundant in the Milky Way galaxy with mean of -1.56. For the metal rich, the median is approximately -0.52. This histogram was reconstructed from the data avaliable in [Harris 1996].

Figure 1.2 shows the distribution of clusters' metallicities. The two subpopulations are clearly identified and this fact constitutes the first clue to propose that each subpopulation has its proper origin. To reinforce the previous claim, the subpopulations are segregated by spatial distribution and kinematic properties. MRGC are axially symmetric distributed near the disc and the galactic bulge: those close to the disc are rotating with it and those near to the bulge have kinematics similar to the random motions of bulge stars. MPGC are distributed spherically symmetric through the stellar galactic halo with random velocities, some of them near the galactic disc and some of them so much far away [Harris 1999]. Figure 1.3 shows the projected position in the sky, in galactic coordinates, of the two subpopulations. The spread in galactic latitude is clearly higher for metal poor subpopulation since they are found in all directions.

Besides the strong correlation between metallicity and spatial distribution, there is another remarkable correlation between the metallicity and the age of the clusters. When the ages of the two subpopulations are compared, a significant number of

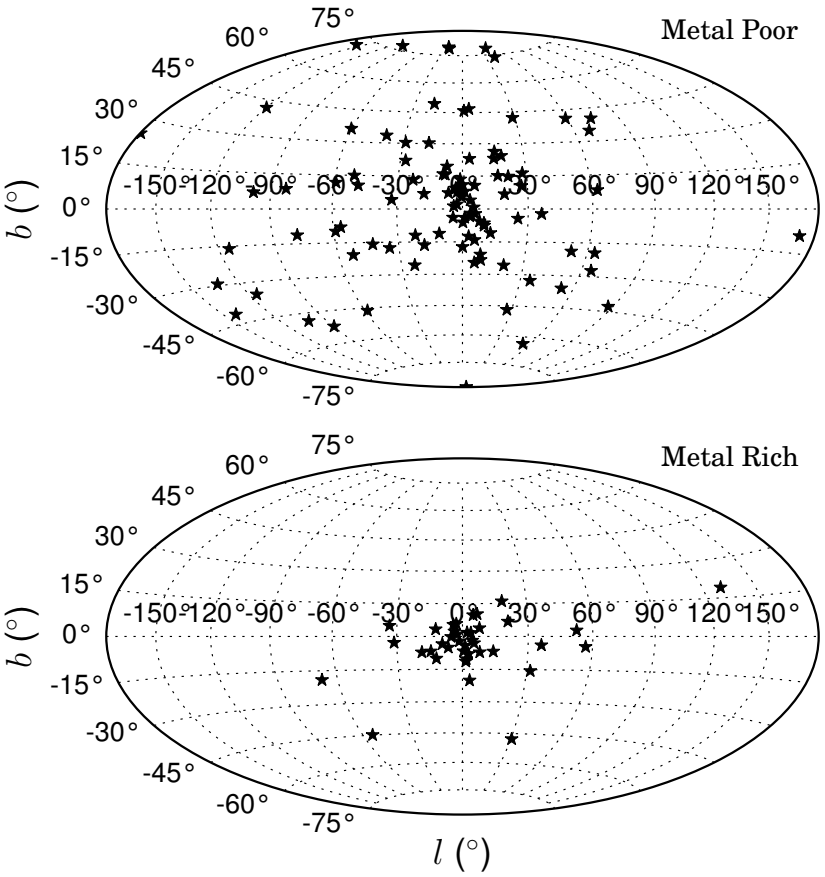

Figure 1.3: Location on the sky in galactic coordinates of the subpopulations of globular clusters in the Milky Way galaxy. This plot was constructed using data of [Harris 1996].

MRGC are significantly younger than most of the MPGC [Shapiro 2010].

However, there is a not negligible number of clusters that break the trend, extremely old with relatively high metallicities. Figure 1.4 illustrates the pair of features discussed in the previous paragraph, extending the discussion to the Andromeda (M31) spiral galaxy where extremely young clusters (∼1 Gyr) have the higher metallicity of all the clusters in Andromeda. Moreover, segregation by metallicity between populations of clusters is not an exclusive peculiarity of the Local Group. Spectroscopic observations of the galaxies in the Virgo Cluster strength the idea that segregation by metal content is a universal characteristic of the globular cluster systems as a natural consequence of the hierarchical galaxy formation process (see [Shapiro 2010] and references therein). It is worth mentioning that this observations are biased by

the technological limitations concerning to the spectroscopic and photometric study of distant objects. More accurate observations can reveal more correlations in globular clusters systems in Andromeda and in galaxies beyond the Local Group. All these facts point directly to conclude that there must be at least two different physical mechanisms by which a globular cluster can be born. For the Old MPGC subpopulation the widely accepted hypothesis is that they come from primordial density fluctuations in the density field at very high redshift, when the universe expanded and cooled to a temperature of about 4000K and the baryonic density was approximately 10^4 atoms cm^3. Under this conditions, the only density fluctuations that can grow with time has wavelength in excess of the critical Jeans length of about 5 pc [Peebles 1968].

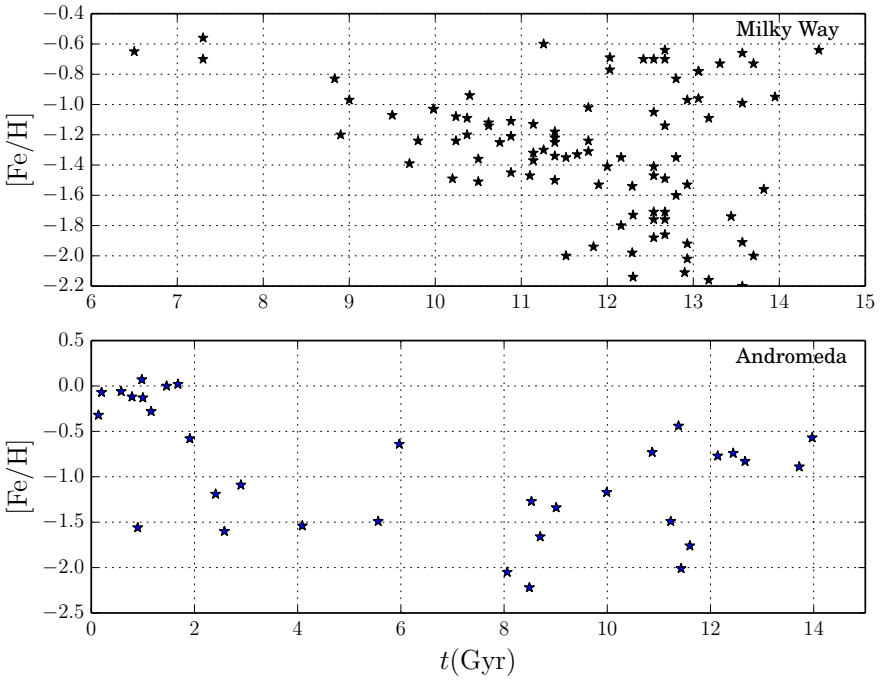

Figure 1.4: Age *vs* Metallicity plot for Globular Cluster Systems of the principal galaxies of the Local Group. For the Milky Way there is a clear tendency of increasing metallicity with decreasing age, except for the old metal rich clusters in the upper right corner. Andromeda shows that the youngest clusters are the metal rich ones, which metallicities are higher even than the metallicity of the Sun. Data from [Forbes 2010] and [Cezario 2013].

The bound protoglobular gas cloud would eventually reach a mass of about $10^5 M_\odot$ to became Jeans unstable, collapsing and fragmenting into the clump that will conceive the individual stars.

The previous model fits quite accurately the lack of heavy elements in the ancient clusters, also suggesting that those clusters that are old and metal-rich must increase their metallicities after its formation, by some external source or by supernovae of very massive stars in its interior [Peebles 1968]. Today many people believe that all old globular clusters in the MW and in any other galaxy originated in this way.

The formation of the young subpopulation still remains as an open issue. Models have been proposed but it appears that there is not a single mechanism that can form all existing MRGC in a given galaxy. One of the main models suggests that a significant fraction of the metal-rich subpopulation may have originated in interacting galaxies, both minor and major mergers [Ashman 1992]. Major mergers cause several starburst episodes in the gaseous component of each galaxy, and globular clusters can be formed in regions with high gas density [Li 2004]. Minor mergers may also contribute to the young population with clusters formed within the small satellite galaxy from the interaction with the larger galaxy [Zepf 1993] Also, the globular cluster system of the minor galaxy would eventually be accreted by the largest galaxy, also contributing to the MPGCs subpopulation [Forbes 2010]. The minor merger scenario can be seen in the Magellanic Clouds, where there is observational evidence of ongoing cluster formation and an ancient cluster system bound to the clouds [Harris 1998]. It was further suggested that a satellite galaxy can generate globular clusters by tidal stripping caused by the larger galaxy, along the orbital motion of the satellite the tidal forces will despoil the stars of the outermost layers of the satellite, finally leaving the core of the satellite galaxy, the new globular cluster [Bekki 2002].

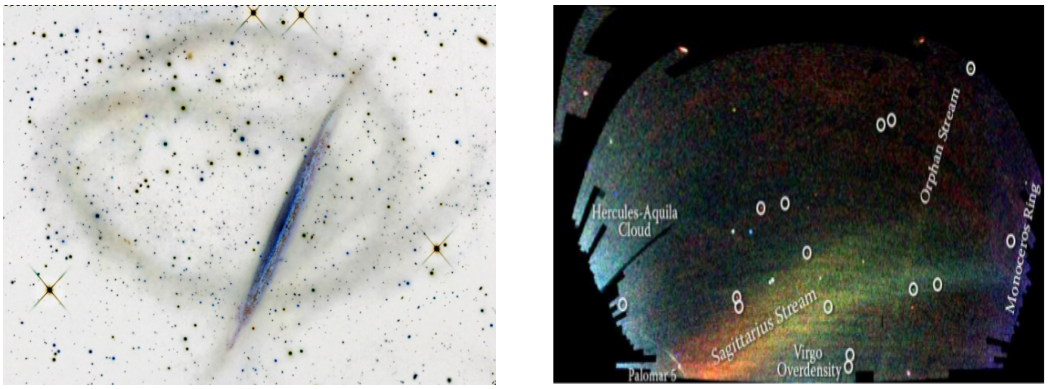

(a) Stream in NGC 5907 (b) The Field of Streams

Figure 1.5: (a) Inverted color image of the streams of stars and gas around the spiral galaxy NGC 5907 seen edge-on [Martinez-Delgado 2010]. (b) The *Field of Streams*. Spatial density of SDSS stars with $g - r < 0.4$ around the north galactic pole. Stand out clearly Sagittarius, Monoceros and Orphan streams and some other overdensities in the MW halo. [Belokurov 2006]

Another model proposed to explain the origin of the metal rich subpopulation argues that super star-forming clumps had optimal conditions to form metal-rich globular clusters. These clumps are massive associations of gas ($10^9 M_\odot$) formed in turbulent gas-rich discs that spiral to the center of the galaxy via dynamical friction, forming the primeval bulge and leaving gas dispersed all across the disc which would form the new clusters [Shapiro 2010].

While all previous models really help to explain the origin of many of the metal-rich clusters, they do not account for the origin of all of them. Major mergers are unable to explain the range in ages and metallicities of the metal-rich clusters since a very large fraction of these events would be required to explain the number of metal-rich clusters, which is why neither minor merger hypothesis is entirely satisfactory [Harris 1998]. On the other hand, only a small number of clusters have the range in stellar ages and metallicities that resemble the core of a satellite galaxy. Star forming clumps are a particular episode of galaxy formation in a very specific time of the evolution of each galaxy, therefore they are inconsistent with the dispersion of cluster's age and also restricts the MRGCs to the galactic disc.

Despite the objections of the model of minor mergers, the purpose of this work is to revisit it and complement it in order to achieve a complete picture of the formation of the metal-rich subpopulation. Here we propose consideration of tidal streams as progenitors of young, metal rich globular clusters. When a satellite galaxy interacts with a larger galaxy, the gravitational potential of the second one acting over the extended body of the first one, slowly removes stars, gas and dust from the satellite that will orbit the larger galaxy in a new stellar structure known as a tidal stream. The gas may eventually agglomerate into different parts of the stream, forming clumps that satisfying some conditions could ultimately form globular clusters at different moments of the galaxy evolution and with a wide range in metallicities, as observed.

This manuscript is organized as follows: Chapter 2 summarizes the main observational and theoretical concepts involved in the formation and evolution of globular clusters and tidal streams, as well as a review of the numerical techniques used to simulate those astrophysical systems. Chapter 3 is the exposure of numerical experiments performed and the procedures used for the analysis of the computational simulations carried out in this work. Finally, Chapter 4 contains the main results obtained in this work, in other words, the principal characteristics of the objects that were identified to be or to form young globular clusters.

Chapter 2

Theoretical Framework

Contents

2.1 Globular Clusters 7
2.1.1 Observations 8
2.1.2 Formation 11
2.1.3 Internal Dynamics 13
2.1.4 External Dynamics 16
2.2 Formation Scenarios of Metal-Rich Globular Clusters 18
2.2.1 Globular Cluster from Galaxy Interactions 18
2.2.2 Globular Cluster from Minor Mergers 18
2.2.3 Globular Cluster from Super Star Formation Clumps 19
2.2.4 Globular Cluster from Turbulent Molecular Clouds 19
2.3 Tidal Streams 20
2.3.1 Observations 20
2.3.2 Formation and Evolution 20
2.4 Simulations 21
2.4.1 *N*-Body Simulations 21

The purpose of this chapter is to present the general existing facts and concepts on all the components involved in this work. The first two sections are devoted to globular clusters and tidal streams and are organized as follows: The first part of each section shows the most important observational facts of each stellar system, while the second part is devoted to the different theoretical aspects concerning the origin and evolution of them. Finally, we describe the computational methods implemented for the simulation of the astrophysical systems studied here.

2.1 Globular Clusters

As it was exposed in the Introduction, the main interest of this reserch are the globular clusters that orbit a galaxy. In this section we summarize the principal results in the research field of globular cluster. We began by describing the overview of the Globular Cluster System besides the observations for individual clusters. The theoretical aspects that govern the dynamics of an individual cluster are reviewed below.

2.1.1 Observations

2.1.1.1 Color-Magnitude Diagrams

The fundamental observational tool for the study of the clusters is the color photometry, through which can be built *Color-Magnitude Diagrams* (CM diagrams). These diagrams are constructed measuring the color indexes and the absolute magnitudes of each star in the cluster. CM diagrams present all evolutionary stages of the stars in each particular cluster. In the bottom of the diagram, are the main sequence stars (MS) with small masses that burn hydrogen in their cores. Going from the bottom end of the diagram to the top-left, more blue, hot and massive stars are located, up to the point where the stars exhaust the hydrogen in their cores, rapidly passing to the subgiant branch (SGB) expanding its outer layer due to the energy liberated by the collapse of the star under its self gravitation [Harris 1998].

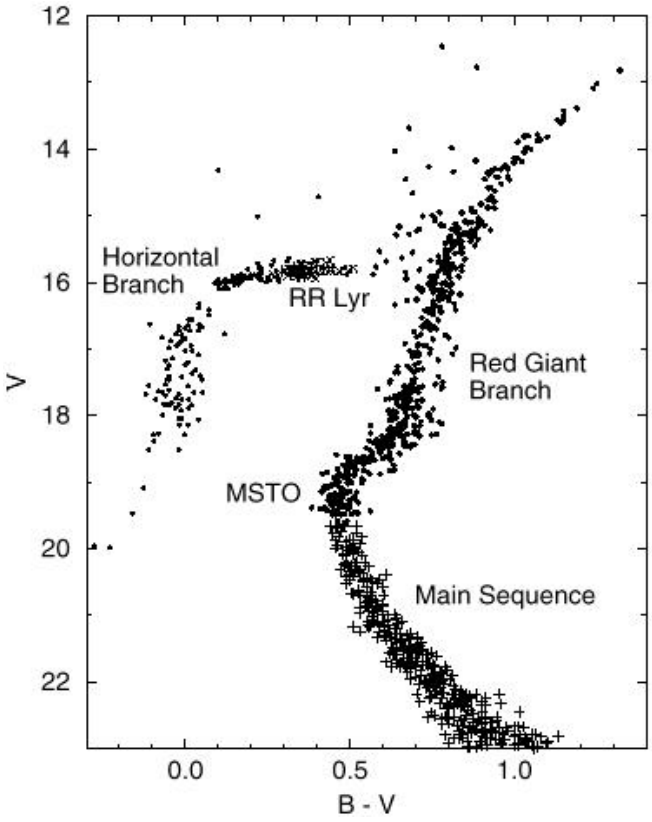

Figure 2.1: Color-magnitude diagram for the globular cluster M15. Plot extracted from [Durrell 1993].

The point of hydrogen exhaustion is known as the *turnoff point* (MSTO) which is fundamental for age estimates of the clusters as it will be discussed soon.
Once a star has reached the subgiant branch, it transit rapidly upwards to the right into the red giant region, becoming redder and cooler, with a diameter that can be

of the order of 1000 times its initial radius.
In the red giant stage, the nucleus of the star becomes increasingly dense and hot (Up to 10^5 g cm^{-3} and 5×10^7 K), igniting the triple alpha process converting helium into carbon. Consequently, the central region expands and the envelope contracts, locating the star in the *horizontal branch*. *RR Lyrae* are distinctive stars of the horizontal branch of each cluster characterized for undergoing pulsations approximately every half a day due to radial instabilities in their envelopes [Lightman 1978].

2.1.1.2 METALLICITY

As it has been noticed so far, to determine the contents of heavy elements in the stars of a cluster is a measure of fundamental importance in the current view of the formation and evolution of its constituent stars, the cluster themselves, their host galaxies and even the large-scale structure. Through metallicity, the age of the clusters is estimated, it is used too to define the characteristics of stellar populations in the clusters, the metallicity distribution function of the Globular Cluster System (GCS) is a key element in the evolution of the galaxy that hosts the System. The metal poor subpopulations of the GCSs may retain traces of the Big Bang nucleosynthesis, making their metallicities unique cosmological tests [Carney 1998].
Metallicity Z is defined as the fraction of mass of an astrophysical object of all elements heavier than helium, with mass fraction denoted by Y. Hydrogen mass fraction is represented by X, so that $X+Y+Z=1$ [Binney 2008]. Usually, metallicity is expressed as the logarithm of the ratio of metal abundance compared to the metal abundance of the Sun. In the case of iron, for example

$$[\mathrm{Fe/H}] = \log\left(\frac{N_{\mathrm{Fe}}}{N_{\mathrm{H}}}\right)_{\bigstar} - \log\left(\frac{N_{\mathrm{Fe}}}{N_{\mathrm{H}}}\right)_{\odot}, \tag{2.1}$$

where N_{Fe} and N_{H} are the number of iron and hydrogen atoms per unit volume respectively [Rowlett 2005]. Iron is not the most abundant heavy element, but is the easier to determine through spectroscopic measures in the visible spectrum. Iron abundance is also related with the abundance of all elements heavier than helium by the expression

$$\log\left(\frac{Z_{\bigstar}/X_{\bigstar}}{Z_{\odot}/X_{\odot}}\right) = A\times[\mathrm{Fe/H}], \tag{2.2}$$

with A taking values between 0.9 and 1 [Rowlett 2005]. Measure of abundances can be performed through several methods from spectroscopic or photometric data. Perhaps the most widespread method is the so-called "ΔS" method based in the comparison of the strenghts of ionezed calcium K line with the hydrogen line at the visual light minimum of the RR Lyrae pulsating stars. Then, the ΔS is defined as the difference between the two line types reckoned in units of tenths of spectral class, denoted as Sp(X) with X any element of interest

$$\Delta S = 10[\mathrm{Sp(H)} - \mathrm{Sp(K)}]. \tag{2.3}$$

Hydrogen spectral line is independent of heavy element contents, therefore it is practically unchanged throughout the stars in the cluster, while the K line is highly

sensitive to metallicity [Carney 1998]. Using high resolution spectra it can be obtained a relationship between [Fe/H] and ΔS

$$[\mathrm{Fe/H}] = (-0.211 \pm 0.013) \cdot \Delta S - (0.065 \pm 0.078), \tag{2.4}$$

different calibrations of ΔS *vs.* [Fe/H] yields different relationships, although all of them remain very similar [Carney 1998].

2.1.1.3 Distances

There are several methods to estimate the distances to globular clusters from photometric data. The first technique consists in the fitting to a fiducial branch of nearby stars of known distance and luminosity. Specifically, the main-sequence of the cluster is fitted to local halo subdwarfs with known metallicities and accurate parallaxes. Given a collection of subdwarfs, the visual magnitude M_V of each star in the set is adjusted by an amount ΔM_V for several sample corrections as the binary nature of some of the subdwarfs or the effects on the parallax measurement from distant stars. Next, the color index is adjusted by $\Delta(B-V)$ to eliminate the metallicity and reddening difference between the cluster and the subdwarfs sample [Harris 1998]. The distance modulus of the cluster is obtained by averaging the shift of a cluster fiducial sequence made to match with the M_V of the subdwarf sample [Durrell 1993]. The distance d of the cluster from Earth is given in parsecs by

$$d = 10^{(m-M)_V+1}. \tag{2.5}$$

RR Lyrae are also widely used for distance determination given that its intrinsic luminosities cover a narrow range of 40-50$\mathrm{L}_\odot$. Be standard candles have revealed that the RR Lyrae variables have a brightness that depends on the fractions Y and Z through the following expression [Carney 1998]

$$M_V(\mathrm{RR}) = \alpha[\mathrm{Fe/H}] + \beta. \tag{2.6}$$

There is a set of methods to determine the coefficients α and β (statistical parallax, GC MS Fitting among others), by means of which the distance modulus of the cluster can be computed [Durrell 1993].

2.1.1.4 Ages

The age of a globular cluster is determined via spectroscopic and photometric data of the stars of the clusters. The relation between cluster age and abundances and the luminosity of the turn-off point L_{TO} is obtained by tracing isochrones on the CMD, these isochrones are constructed from models of stellar evolution and given that all cluster stars were formed about the same time, the age of the cluster T_g is calculated by the interpolation equation [Sandage 1970]

$$\log T_g = \frac{\log L_{\mathrm{TO}}/L_\odot + (0.92 + 0.11\log Z)Y + 0.219\log Z - 0.789}{0.10\log Z - 0.59}. \tag{2.7}$$

The luminosity of the turn-off point is estimated from the visual absolute magnitude M_V^{TO} in the CMD. This magnitude has to be corrected to obtain the bolometric magnitude of the turn-off point $M_{\mathrm{bol}}^{\mathrm{TO}}$ from which it can be found the bolometric luminosity of the turn-off point L_{TO}

$$\log L_{\mathrm{TO}}/L_{\odot} = (M_{\mathrm{bol}}^{\odot} - M_{\mathrm{bol}}^{\mathrm{TO}})/2.5. \tag{2.8}$$

Helium abundance can also be estimated from the CMD through another formula obtained by interpolation [Sandage 1970]

$$Y = 1.6(B-V)_{\mathrm{BE}} - 0.34\mathcal{M}/\mathcal{M}_{\odot} - 0.16M_V + 0.901, \tag{2.9}$$

with $(B-V)_{\mathrm{BE}}$ the color at the blue edge of the RR Lyrae strip, M_V and $\mathcal{M}$ are respectively the corresponding absolute magnitude and mass at the edge. The blue horizontal edge masses are approximately related with its metallicities by the relation [Sandage 1993]

$$\log \mathcal{M} = -0.059[\mathrm{Fe/H}] - 0.288, \tag{2.10}$$

thereby, the recipe to estimate the age of the clusters is completed.

2.1.2 Formation

2.1.2.1 Gravitational Collapse and Fragmentation

The formation of stellar clusters begins when molecular clouds meet the conditions for giving birth to a new group of stars. Therefore, the first step is to understand how the star formation process operates in this clouds.
Interstellar molecular clouds can be regarded as stable, gravitationally bound systems. The average kinetic energy $\langle K\rangle$ of the cloud and the average potential energy $\langle U\rangle$ of each particle satisfy the virial theorem. In its simplest version, the virial theorem can be written as [LeBlanc 2010],

$$2\langle K\rangle + \langle U\rangle = 0. \tag{2.11}$$

This virial equilibrium can be broken by different mechanisms, causing the transformation of the cloud into a new astrophysical object. If the main kinetic energy is large enough to overcome the gravitational balance between the particles of the cloud, two scenarios are possible. In the first the cloud will expand but will find the virial equilibrium after some time. In the second, improbable scenario, the kinetic energy of the particles will be so large that definitely depart from each other enough to become unbounded, destroying the cloud. If, however, the movement of the particles is not large enough to counteract the gravitational forces, the cloud will collapse. This means that the gravitational collapse occurs when the cloud mass has exceeded a certain critical value, which is known as the Jeans mass, which in turn depends on the temperature T and density ρ of the particular cloud. Considering that the cloud can suffer external pressures, the Jeans mass can be written as

$$M_J = \left(\frac{3}{4\pi\rho}\right)^{1/2}\left(\frac{5k_BT}{\mu m_H G}\right)^{3/2}, \tag{2.12}$$

where k_B is the Boltzmann constant, m_H is the mass of the hydrogen atom, assuming a cloud mostly made of H and μ is the cloud mean molecular weight [Draine 2011]. As the cloud collapses, its density increases and thus the Jeans mass decreases. The collapse process is isothermal because the energy is radiated away from the collapsing cloud and the temperature is maintained approximately constant. As a result, any inhomogeneity within the cloud outweigh the increasingly smaller Jeans mass and begin to collapse themselves. At some point, the cloud becomes opaque, radiation can not scape the cloud and then the collapse of the cloud is stopped because the process becomes adiabatic, storing all the energy and allowing the temperature to grow [Carroll 2007].
Equation 2.12 indicates that $M_J \propto \rho^{-1/2}$ in the isothermal regime. When the regime becomes adiabatic and the temperature starts to grow with the increasing pressure P of the cloud, $T \propto P^{2/5}$. Through the equation of state, $P \propto \rho T$, it can be concluded that the temperature depends on the density as $T \propto \rho^{2/3}$, resulting in a growing Jeans mass given that in this regime $M_J \propto T^{3/2}\rho^{-1/2} \sim \rho^{1/2}$. Then, when the rate of binding energy which heat the gas during the collapse is approximately equal to the rate of radiation loss by the gas, the fragmentation stops. Under the foregoing conditions, the mass M_{frag} when the fragmentation has reached its limit is found to be

$$M_{\text{frag}} \approx 0.02 M_\odot \frac{T^{1/4}}{f^{1/2}}, \tag{2.13}$$

with f a radiation emission efficiency factor less than 1 since the cloud always emit less radiation than a black body. Assuming reasonable ranges for T ($\sim$ 1000K) and f ($\sim$ 0.1), it is concluded that fragmentation terminates if the fragments are of the order of the solar mass, independent of the redshift or chemical composition [Kippenhahn 2012].
Nonlinear phenomena present in the dynamics of the molecular clouds (turbulence, radiative MHD shocks and others) also play a role in the stellar formation, it prevents the global collapse of the clouds to create instead a collapse in highly anisotropic filaments. These filaments form dense cores with large density contrasts [Chabrier 2003] in which stars could form. The environment of the molecular giant clouds is decisive for the resulting post-collapse structure. The mass of the clouds and the pressure exerted by the surrounding environment directly affects the efficiency of star formation. High pressure environments as galactic halos, interacting galaxies, and the dense cores of molecular clouds in dwarf galaxies should end up dense and gravitationally bound, like globular clusters. Clusters that form in moderate to low pressure environments end up as unbound expanding stellar associations [Elmegreen 1997].

2.1.2.2 Initial Mass Function

It is essential to know how many regions can then collapse in a cloud of a given mass. To do this we can adapt the Press-Schecter formalism for this non-cosmological scenario. Roughly speaking, the number of elements of mass with a mass larger than the Jeans mass, could be calculated assuming that the inhomogeneities in

the density of the cloud are gaussian distributed and adopting the ansatz that at any given point the probability that an inhomogeneity is larger than the Jeans mass is equal to the fraction of regions that have masses greater than the Jeans mass [Mo 2010]. The overdensity field is defined as

$$\delta(\mathbf{r},t) = \frac{\rho(\mathbf{r},t) - \overline{\rho}}{\overline{\rho}}, \tag{2.14}$$

with $\overline{\rho}$ the mean density of the cloud. If we construct a smooth gaussian density field δ_s , the probability that at some point δ_s has a value larger than the associated Jeans density δ_J at that point is given by

$$P(\delta_s > \delta_J) = \frac{1}{(2\pi)^{1/2}\sigma(M)} \int_{\delta_J}^{\infty} \exp\left[-\frac{\delta_s^2}{2\sigma^2(M)}\right] \mathrm{d}\delta_s, \tag{2.15}$$

where the mass dispersion $\sigma(M)$ needs to be specified in this case. Once the value of the dispersion is found, the Press-Shechter ansatz ensures that if $F(M > M_J)$ is the fraction of masses greater than the Jeans mass, its value will be $F(M > M_J) = P(\delta_s > \delta_J)$ and the number of objets with masses between M and $M + \mathrm{d}M$, $N(M)\mathrm{d}M$ at a given time can be calculated with the expression

$$N(M)\mathrm{d}M = -\frac{\overline{\rho}}{M}\frac{\partial F}{\partial M}\mathrm{d}M \tag{2.16}$$

$$= 2\frac{\overline{\rho}}{M}\frac{\partial P}{\partial \sigma}\left|\frac{\mathrm{d}\sigma}{\mathrm{d}M}\right|\mathrm{d}M. \tag{2.17}$$

$N(M)$ is known as the mass function. As stars evolve along the main sequence, the mass function evolves from its initial form or initial mass function ϕ (IMF). The present day mass function ξ (PDMF), that is, the number density distribution per mass interval at the present time is determined directly by the observed present day luminosity function, and the number of stars formed per time interval along galactic evolution, the star formation rate $b(t)$ (SFR) satisfies the condition [Chabrier 2003]

$$\phi(\log M) = \frac{\xi(\log M)}{\tau_G} \int_{\tau_G - \tau_{MS}}^{\tau_G} b(t)\mathrm{d}t, \ \tau_{MS} < \tau_G, \tag{2.18}$$

where τ_G is the age of the cluster and τ_{MS} is the lifetime of Main Sequence stars. Observational studies have concluded that the PDMF for globular cluster is consistent with a lognormal distribution peaked at $M_c = 0.33 \pm 0.03\mathrm{M}_\odot$ with standard deviation $\sigma = 0.34 \pm 0.04$ [Chabrier 2003]:

$$\xi(M) \propto M^{-1}\exp\left\{-\frac{(\log M - \log M_c)^2}{2\sigma^2}\right\}. \tag{2.19}$$

2.1.3 INTERNAL DYNAMICS

As for any bound stellar system, the dynamical evolution is determined by the gravitational scatterings between stars within the system. The motion of the stars

is therefore determined by the close encounters between stars and the effect of more distant stars of the clusters. Close encounters produce large deflections and velocity changes, but still remain significantly smaller than the acceleration produced by the complete particle distribution, as will be seen below.

2.1.3.1 Characteristic Timescales

The relaxation time t_r measures the time required for collisions to produce large changes in the initial velocity distribution. After a time interval t_r, the N-body bound, gravitating system would reach quasi-Maxwellian equilibrium in its interior. Assuming that all of the N stars in the cluster have equal mass m, with mean square velocity v_m^2 and local star density n, the relaxation time is estimated by the expression

$$t_r = \frac{v_m^3}{\pi G^2 m^2 n \ln(0.5N)}, \tag{2.20}$$

where G is the gravitational constant. The dynamical timescale t_d is usually defined as the elapsed time during the displacement of a star with the rms velocity over a characteristic scale length, as for instance, the radius containing half of the cluster mass, R_h. Namely, t_d is simply given by

$$t_d = \frac{R_h}{v_m} = \frac{\sqrt{2} R_h^{3/2}}{(GM)^{1/2}}, \tag{2.21}$$

where M is the total mass of the cluster. By employing the virial theorem, we can write the relation $v_m = GM/2R_h$, which combined with the definitions $m = M/N$ and $n = N/(4\pi R_h^3/3)$ allows the comparison between the two time scales, ie

$$\frac{t_d}{t_r} \approx \frac{3\ln(0.5N)}{N}. \tag{2.22}$$

For globular clusters $10^4 \leq N \leq 10^6$, this is, the relaxation time is several orders of magnitude greater than the dynamical time, therefore, a star can orbit the stellar system several hundreds of times at least before its energy and angular momentum change appreciably. Furthermore, the age of the clusters is larger than the relaxation times, making the clusters relaxed N-body systems by two-body encounters, ultimately resulting in the equilibrium velocity profiles observed in globular clusters [Lightman 1978].

2.1.3.2 Core and Tidal Radii

Globular clusters have a core-halo structure with a highly concentrated core, with densities up to $10^6 \mathrm{M}_\odot/\mathrm{pc}^3$. The density decreases significantly in the surrounding halo. To characterize this structure for a given cluster, two distances for each cluster are generally used, besides the half-mass radius defined in the previous section, one usually defines the core r_c and tidal r_t radii.
Core radius corresponds to the radius at which the density drops to one third of its

central value (ρ_c). Observationally it is equivalent to the radius at which the surface brightness drops to half of its central value. The virial theorem applied to the core of the globular cluster defines the core radius through the equation [Benacquista 2013]

$$v_c^2 = \frac{4\pi G}{3}\rho_c r_c^2, \tag{2.23}$$

where v_c^2 is the mean-squared central velocity.
On the other hand, r_t is related to the place where the gravitational field of the host galaxy becomes larger than the self-gravitation of the cluster distribution, there the tidal radius r_t has been reached. Taking into account several considerations, as the point masses approximation and the cluster circular orbit, a rough estimate of the tidal radius of a cluster of mass M is [Spitzer 1987]

$$r_t^3 = \frac{M}{2M_{\mathrm{GAL}}}R_{\mathrm{GAL}}^3, \tag{2.24}$$

where M_{GAL} is the total mass of the galaxy enclosed by the galactocentric distance of the cluster R_{GAL}, including host halo's dark matter.

2.1.3.3 Violent Relaxation and Mass Segregation

Once the cluster is recently formed, the nature of the system is permanently changed. The primordial cloud is now an association of less, more massive bodies, as large amounts of gas particles have become stars due to fragmentation. The relaxation time of the system is therefore significantly reduced. As a result of this situation, the positions, velocities and masses of the stars will be initially uncorrelated. This initial phase of the cluster evolution is known as the *violent relaxation* in which the energy of each star changes in a mass-independent manner.

The system will undergo damped oscillations of the total energy, after which the systems reaches a violently relaxed quasiequilibrium configuration [Lightman 1978].

Meanwhile equilibrium is established in the system, equipartition of energy causes the transference of kinetic energy from the most massive stars to low mass stars through two-body encounters. Most massive stars consequently fall to the core of the cluster leaving the less massive stars in the periphery. This *mass segregation* process is accomplished in roughly one relaxation time [Spitzer 1987].

2.1.3.4 Gravothermal Instability

Gravitationally bound systems have negative heat capacities as a consequence of its virialization. Virial theorem 2.11 ensures that $\langle K\rangle = -\langle U\rangle/2$, secondly, the dynamical temperature of the cluster is define by

$$\langle K\rangle = \frac{3}{2}Nk_BT, \tag{2.25}$$

with k_B the Boltzmann constant. Therefore, the total internal energy for the cluster will be

$$\langle E \rangle = -\frac{3}{2} N k_B T, \tag{2.26}$$

thereby defining the heat capacity as

$$C = \frac{\mathrm{d}\langle E \rangle}{\mathrm{d}T} = -\frac{3}{2} N k_B. \tag{2.27}$$

Self-gravitating systems lose energy when heated. In the core of the cluster, the massive stars are concentrated making it a much more strong self-gravitating system than the halo. Halo can therefore be considered as a heat bath for the core [Spitzer 1987]. Eventually, any external perturbation will cause a loose of energy of the core to the outer regions, heating up and contracting in the process. The increasing kinetic energy will cause additional flow of heat from the core to the surrounding regions, shrinking the core even more in a runaway process called *gravothermal catastrophe*. The contraction of the cluster is know as *core collapse* [Benacquista 2013]. The central density of the cluster increases for several orders of magnitudes due to the accelerated collapse. The formation and evolution of binaries and their three-body interactions would be more frequent and stronger as the collapse is carried out and eventually their binary heating does start to influence the collapse rate, quickly thereafter reversing the collapse in an expansion of the central region [Cohn 1989]. As the core expands, its outer layers will be in contact again with the cool halo and the instability will be back, contracting the core until binary heating reverse the process over again. These *gravothermal oscillations* will be present during most of the lifetime of the cluster.

2.1.4 External Dynamics

The evolution of a globular cluster as a whole will be determined by the environment in which it is formed. The components of the host galaxy to which the cluster is bound dictate the movement of the cluster and also influence the internal dynamics of its stars and gas. In the following, we review the main mechanisms involved in the orbital motion of the clusters around its host galaxy.

2.1.4.1 Tidal Stripping

Globular clusters orbit the host galaxy under the influence of the host gravitational potential. During their journey, clusters experience the action of the potential over the entire length of their bodies. The additional acceleration upon each star could eventually overcome the gravitational field of the cluster at the position of the star, releasing it of the cluster to become a star of the galactic halo. As discussed in section 2.1.3.2, stars that are farther away from the tidal radius would be the ones stripped out. Along the orbital motion of the cluster, tidal radius changes with the distance of the cluster to the center of the galaxy, being minimal at the perigalacticon where the host potential over the cluster is the strongest.

The stars that remain bound to the cluster are also distributed by the galactic potential. The change in energy due to the external potential is known as the tidal heating of the cluster. The total heating is the contribution of the heatings generated by the components of the galaxy, each manifesting as the cluster orbits the galaxy. Disk heating dominates when the cluster passes through the galactic disk and bulge heating is the predominant when the cluster passes close to the galactic center. There is several analytical calculations for the tidal heatings of each component, but in general, tidal heating ΔE of a N-body system due to an external potential is estimated by [Binney 2008]

$$\Delta E = \frac{1}{2}\sum_{i}^{N} m_i |\Delta \mathbf{v}_i|^2, \tag{2.28}$$

where the sum is extended over all cluster particles of mass m_i and velocity $\mathbf{v}_i$.

2.1.4.2 DYNAMICAL FRICTION

The Globular Cluster System is embedded in the dark matter halo of the host galaxy. While each cluster traverses its orbit, transfers orbital kinetic energy to the dark matter by which the cluster is going through. In other words, the dark matter left behind the cluster gravitationally attracts it causing a gradual slowndown. The deceleration is reflected in the orbital decay of the cluster to the galactic center in a spiral trajectory.
If the cluster of mass M is traveling with velocity $\mathbf{v}$ through the dark matter halo with particles of mass m_i ($m_i \ll M$) and isotropic velocity distribution $f(v_i)$, the drag force can be obtained from the Chandrasekhar's dynamical friction formula. Here we enunciate the drag force for the case of relaxed dark matter in which the velocity distribution of the dark matter particles is Maxwellian with dispersion σ [Binney 2008].

$$\frac{\mathrm{d}\mathbf{v}}{\mathrm{d}t} = -\frac{4\pi G^2 M \rho \ln\Lambda}{v^3}\left[\mathrm{erf}(\chi) - \frac{2\chi}{\sqrt{\pi}}\mathrm{e}^{-\chi^2}\right]\mathbf{v}, \tag{2.29}$$

where ρ is the mass density of the scattered bodies and $\chi \equiv v/(\sqrt{2}\sigma)$. The Coulomb logarithm $\ln\Lambda$ for a extended spherical body orbiting a host galaxy of mass M_{GAL} and radius R_{GAL} is

$$\ln\Lambda = \ln\left(\frac{b_{\max}}{\max(R_h, MR_{\mathrm{GAL}}/M_{\mathrm{GAL}})}\right), \tag{2.30}$$

R_h is the half-mass radius of the cluster and $b_{\max}$ is the maximum impact parameter. Averages values for clusters are $R_h = 3\mathrm{pc}$ and $b_{\max} = 1\mathrm{Kpc}$, yielding $\ln\Lambda = 5.8$. Chandrasekhar's formula allow the estimation of the time t_{sp} spent by the cluster to reach the center of the galaxy from a distance r_i [Binney 2008]

$$t_{\mathrm{sp}} = 64\mathrm{Gyr}\frac{\sigma}{200\mathrm{kms}^{-1}}\left(\frac{r_i}{1\mathrm{kpc}}\right). \tag{2.31}$$

2.1.4.3 Ram pressure stripping

The galactic halo contains also large amounts of gas, leftover of the galaxy formation process and amounts are added later by accretion of intergalactic gas or satellite galaxies. This halo gas exerts pressure $P_{\rm ram}$ over the interstellar medium of the traversing bodies. If $\rho_{\rm gas}$ is the density of the halo gas, v is the velocity through the gas of a cluster with gas density ρ and velocity dispersion σ, then, for ram-pressure stripping to occur, it must be satisfied that [Gunn 1972]

$$P_{\rm ram} = \rho_{\rm gas} v^2 > \frac{\sigma^2 \rho}{3}. \tag{2.32}$$

When the previous condition is met, ram-pressure will strip out a large fraction of the cluster gas and dust.

2.2 Formation Scenarios of Metal-Rich Globular Clusters

2.2.1 Globular Cluster from Galaxy Interactions

Globular clusters seem to be much more frequent in elliptical galaxies than spiral ones, the specific frequency is typically a factor of two higher around ellipticals. Ashman & Zepf [Ashman 1992] proposed that while halo cluster population forms during protogalactic collapse, the disk globular clusters in spirals and the excess around ellipticals are product of accretion or merger events. Specifically globular cluster forms from the available gas mass in the merging galaxies, the star formation is triggered by gas collisions or shocks during the merger. If ε is the efficiency of globular cluster formation, then, the number $N_{\rm new}$ of clusters that form during a galaxy merger is

$$N_{\rm new} \approx 50 \left(\frac{\varepsilon}{10^{-3}}\right) \left(\frac{M_{\rm clus}}{2\times 10^5 {\rm M}_\odot}\right)^{-1} \left(\frac{M_{\rm gas}}{10^{10}{\rm M}_\odot}\right), \tag{2.33}$$

where $M_{\rm clus}$ is the characteristic mass of globular clusters and $M_{\rm gas}$ is the available gas mass in the interacting galaxies. Thus, the excess in ellipticals is explained considering that they come from the merger of spirals with high gas contents.

2.2.2 Globular Cluster from Minor Mergers

Using numerical simulations of minor mergers, Bekki & Chiba [Bekki 2002] showed that the conditions to form compact clusters of stars can be met at central regions of the satellite galaxies tidally interacting with larger host galaxy. They concluded that if the the satellite is a gas-rich one, the pressure in its central region can become so high to induce global collapse of giant molecular clouds. If P_g is the interstellar gaseous pressure, in order to collapse pressure-confined, magnetized, self-gravitating molecular clouds, it has to be larger than the surface pressure P_s of the clouds

$$P_g \geq P_s \sim 2.0 \times 10^5 k_B \ {\rm cm}^{-3}{\rm K}, \tag{2.34}$$

where k_B is the Boltzamnn constant in the cgs unit system. A main result of the model is that the newly formed metal rich clusters are centrally concentrated depending on the orbital initial configuration of the satellite, depending on eccentricity of the satellite galaxy, its relative mass, the inclination and relative direction of rotation. In a subsequent study [Bekki 2003], it was proven that massive clusters like ω-Centauri could form from ancient dwarf galaxies merging within the host galaxy. Numerical simulations showed that the outer stellar envelopes of the dwarf galaxies get almost completely stripped out by tidal forces and ram pressure exerted by the host galaxy, while the nucleus of the core survives to the stripping by its strong self-gravity. This system shows a wide spread in the metallicities and ages of its constituent stars, what appears to be a common feature of the more massive clusters. The conclusion is, therefore, that some young, metal-rich, massive clusters come from *nucleated* dwarf galaxies.

2.2.3 Globular Cluster from Super Star Formation Clumps

Super star forming clumps (SSFC) are vast bodies of gas and dust ($R \sim 1-3$ kpc; $M \sim 10^9 \mathrm{M}_\odot$) with high star formation rates (10-200 $\mathrm{M}_\odot \mathrm{yr}^{-1}$). Around 5-10 of these clumps formed in each galaxy preferably in turbulent gas-rich discs in the clump-driven phase at $z \sim 2$. Dynamical friction caused them to spiral into the center of the galaxy to form a primeval bulge, leaving a fraction of their masses in the star-forming disc. The SSFC form gravitational unstable structures that will form cluster by gravitational collapse. Thus, larger bulges will be indicators of a larger number of clusters, as observed [Shapiro 2010]. The SSGC form 700 structures of 10^{-3} times the mass of the original cloud, this is, stellar systems up to $10^6 \mathrm{M}_\odot$. Of the initial 700, about 10 survive until $z = 0$, giving a total of 50-100 young clusters per galaxy [Shapiro 2010].

2.2.4 Globular Cluster from Turbulent Molecular Clouds

In contrast to the other models, Elmegreen & Efremov argued there is only one universal mechanism by which both the old and young globular clusters are formed [Elmegreen 1997]. The formation of globular cluster is triggered when supersonic turbulence divides the Giant Molecular Clouds into a fractal web structure of density fluctuations that depending in the mass and pressure of the region will transform the clouds in a globular cluster, an open cluster or an association of unbound stars. This mechanism applies for all epochs or cloud's geometries since depends only in the formation efficiency which is nearly constant for clouds under similar conditions. Particularly, globular clusters form in high-pressure environments as the protogalactic halo which originates the old halo clusters. In the same way, the young clusters associated with the galactic disc and bulge form from the high pressure environments created by galactic collisions and interactions [Elmegreen 1997].

2.3 Tidal Streams

2.3.1 Observations

Tidal streams are relatively recently discovered structures because detecting them in the vast field of stars on the sky require high observational performance in order to distinguish them from the enormous amount of foreground native stars of The Galaxy. Chronologically, the first method used was the determination of the direction of motion of a group of stars and compare it with the direction of galactic rotation [Eggen 1971].

The identification of the first groups of stars with particular kinematics and chemical properties laid the foundation to study the origin and evolution of tidal streams. Recently most streams are detected through spectroscopic and photometric methods, for instance, measuring kinematic anomalies of bulge K giants or measuring u, g, r, i, z photometry to map regions of the sky looking for star color overdensities. The application of this technique is depicted in figure 1.5 (b) [Belokurov 2006].

Observations with modest-sized telescopes have been used to study tidal features in spiral galaxies beyond the Local Group. These observations were performed luminance filter and the resulting images clearly show the stellar substructures in the halo of the studied spirals [Martinez-Delgado 2010].

2.3.2 Formation and Evolution

When the gravitational field of a host massive galaxy acts over the extended body of a satellite galaxy, the gravitational force generated varies in different points of the satellite. Therefore, some stars will be accelerated more and eventually become bound to the host galaxy, orbiting it in an orbit similar to that described by the satellite galaxy. With the passing of time, the number of stars undergoing this transition will be longer, forming a large arc-shaped structure around the host galaxy, the tidal so-called stream.

Considering that the halo is distributed spherically, with density $\rho(r)$ where r is the distance to the halo center and with certain approximations, the acceleration over a single star due the host potential can be expressed as, with $\mathbf{r}$ the position of the satellite star relative to the halo center

$$\dot{\mathbf{v}} = -\frac{G}{R^3}\left[(3M - R\dot{M})\frac{\mathbf{R}\cdot(\mathbf{r}-\mathbf{R})}{R^2}\mathbf{R} + M(\mathbf{r}-\mathbf{R})\right], \tag{2.35}$$

where $M = M(R)$ is the mass enclosed in a sphere of radius R and $\dot{M}$ its derivative with respect to R, the distance of the satellite center of mass to the halo center.

The interaction with the halo is the main factor that produces the tidal stream and is also the one that drives the stream evolution over the majority of its lifetime. But, when the satellite galaxies approaches to the galactic disc, it generates strong accelerations that become important in the evolution of the stream. During disc passage, the path of the satellite could be approximated as a straight line path, with mean velocity V_z.

On the other hand, from Poisson's equation, the potential generated by the disc Φ_d of density ρ_d is

$$\frac{\mathrm{d}^2\Phi_d}{\mathrm{d}Z^2} = 4\pi G\rho_d, \tag{2.36}$$

with which it can be obtained the change of energy produced by the disc passage. If the satellite crossing radius through the disc is R, the disc heating is found to be [Binney 2008]

$$\Delta E_s = \frac{8}{3}\frac{\pi^2 G^2 \Sigma_d^2}{V_z^2} R^2, \tag{2.37}$$

where $\Sigma_d(R)$ surface density of the disc.

The heating is strongest at the outer parts of the satellite and is just in this regions of the satellite where the impulse approximation holds because in the inner part, the orbital time may be less than the encounter time. Thus, the disc shocks are an important mechanism for untie the stars of the satellite.
Also, satellite can cross through the galactic bulge. However, the time of the encounter is very large and the impulse approximation is not strictly valid.

2.4 SIMULATIONS

2.4.1 N-BODY SIMULATIONS

The computational simulations in this work are performed using the open source code known as GADGET2 [Springel 2005]. The dynamics of collisionless particles (Dark matter and stars) is described by the hamiltonian

$$H = \sum_i \frac{p_i^2}{2m_i a(t)} + \frac{1}{2}\sum_{ij} \frac{m_i m_j \varphi(\mathbf{r}_i - \mathbf{r}_j)}{a(t)}, \tag{2.38}$$

where $\mathbf{r}_i$ are the coomoving vectors with conjugated canonical momentum given by $\mathbf{p}_i = a^2 m_i \dot{\mathbf{r}}_i$. The temporal dependency is included in the evolution of the scale factor $a(t)$ given by the Friedman-Lamaitre model. In our case, the simulations will be non-cosmological, with $a(t) = 1$ and newtonian flat geometry. The gravitational potential $\varphi(\mathbf{r})$ satisfies the Poisson equation:

$$\nabla^2\varphi(\mathbf{r}) = 4\pi G\rho(\mathbf{r}). \tag{2.39}$$

For the collisional particles (gas), the evolution of the hydrodynamical features is performed by the *Smoothed Particle Hydrodynamics* formalism. The density is estimated as

$$\rho_i = \sum_j m_j W(r_{ij}, h_i), \tag{2.40}$$

according to the kernel function $W(r,h)$ which depends in turn of the smoothing length h. The equation of motion for the collisional particles is writen in terms of W

$$\frac{\mathrm{d}\mathbf{v}_i}{\mathrm{d}t} = -\sum_{j=1}^{N} m_j \left[f_i \frac{P_i}{\rho_i^2} \nabla_i W_{ij}(h_i) + f_j \frac{P_j}{\rho_j^2} \nabla_i W_{ij}(h_j) \right], \tag{2.41}$$

where

$$f_i = \left[1 + \frac{h_i}{3\rho_i} \frac{\partial \rho_i}{\partial h_i} \right]^{-1}, \tag{2.42}$$

with pressures $P_i = A_i \rho_i^{\gamma}$. Without heat sources or shocks, the flux is reversible and the entropy A_i of each particle remains constant.
Temporal evolution of the particles is carried out by a *Leap-Frog* algorithm with temporal evolution operator $U(\Delta t)$ given by

$$U(\Delta t) = D\left(\frac{\Delta t}{2}\right) K(\Delta t) D\left(\frac{\Delta t}{2}\right), \tag{2.43}$$

whose operators "kick", $K(\Delta t)$ and "drift", $D(\Delta t)$ are given by

$$D_t(\Delta t) : \begin{cases} \mathbf{p}_i & \mapsto & \mathbf{p}_i \\ \mathbf{x}_i & \mapsto & \mathbf{x}_i + \frac{\mathbf{p}_i}{m_i} \int_t^{t+\Delta t} \frac{\mathrm{d}t}{a^2} \end{cases} \tag{2.44}$$

$$K_t(\Delta t) : \begin{cases} \mathbf{x}_i & \mapsto & \mathbf{x}_i \\ \mathbf{p}_i & \mapsto & \mathbf{p}_i + \mathbf{f}_i \int_t^{t+\Delta t} \frac{\mathrm{d}t}{a} \end{cases} \tag{2.45}$$

and

$$\mathbf{f}_i = -\sum_j m_i m_j \frac{\partial \phi(\mathbf{x}_{ij})}{\partial \mathbf{x}_i} \tag{2.46}$$

is the force over a particle.

Chapter 3

Numerical Procedures

Contents

3.1 Realization of the isolated galaxies 23
3.1.1 The Host Galaxy 23
3.1.2 The Satellite Galaxy 25
3.2 Numerical Realizations 28
3.3 Initial Positions 29
3.4 Gravitational Potential Evaluation 32
3.5 Density Computation 33

Formation and evolution of globular clusters are astrophysical processes ocurring in cosmological timescales. Therefore, to observe any change in a tiny fraction of these processes for our human limited time scales is practically impossible, becoming essential to study the origin and evolution of globular clusters using computer simulations. In this chapter we present the numerical methods adopted in this work. In section 3.1 the numerical techniques used to set up initial conditions for the galaxies involved in the simulation are discussed, including a description of the aspects concerning the gaseous component of the satellite galaxies in the simulations. Then, in section 3.3 we show the methodology followed to choose the initial relative location of the interacting galaxies and to configure the mergers. In the subsequent sections, we show the different techniques implemented to identify potential globular cluster candidates from the substructures formed in the $N-$Body hydrodynamical simulations. Finally, this chapter ends with the methods applied to the candidates to characterize them and diagnose the kind of astrophysical objects formed.

3.1 Realization of the isolated galaxies

The entire set of simulations consists in the interaction ot two systems, a Milky Way type galaxy or host galaxy and a typical spheroidal satellite galaxy. The center of mass of the host galaxy is always located at the origin of coordinates, while the satellite is located in different initial positions and has no rotation.

3.1.1 The Host Galaxy

The host galaxy was built based on the CLUES project [Gottlober 2010]. This means that we generate a disc galaxy specially conditionated to relive the real Milky

Way in the Local Group according with the ΛCDM model of structure formation. Therefore, the values of the virial mass and radius for the dark matter halo are obtained from the Most Massive Projenitor of the MW at $z \approx 2$ in one of CLUES simulations. The mass distribution of this halo is given by the truncated Hernquist density profile [Hernquist 1993]

$$\rho_{\rm halo}(r) = \frac{M_h}{2\pi}\frac{a_h}{r(r+a_h)^3}, \tag{3.1}$$

where M_h is the halo mass and a_h is the halo's radial scale length which is related with the scalelength r_s of the Navarro-Frenk-White profile via the concentration index c through the expression

$$a_h = r_s\sqrt{2[\ln(1+c) - c/(1+c)]}, \tag{3.2}$$

with $c = r_{200}/r_s$ and r_{200} is defined as the radius in which the mean density of the enclosed dark matter is exactly 200 times greather than the critical density of the universe [Springel 2005]. The values for all the haloes in the simulations we have the following values: $M_h = 7.9 \times 10^{11}{\rm M}_\odot$, $r_{200} = 63.29$ Kpc, $c = 4.15$.

The choice of an Hernquist halo instead of a NFW halo stems basically from two facts. The first one is that the total mass in the Hernquist profile remains finite in the outer parts while the total mass in NFW is divergent. The second one is the equivalence of the profile 3.1 and the NFW profile in the inner regions of the halo [Springel 2005]. The embedded disc has a stellar mass equivalent to the 0.4% of the dark matter halo according to the literature reported values [Moster 2010].

The density distribution for the galactic disc is a combination of the bright distribution in vertical and radial directions [Hernquist 1993]

$$\rho_{\rm disc}(R,z) = \frac{M_d}{4\pi r_d^2 z_0}{\rm sech}^2(z/z_0)\exp(-R/r_d), \tag{3.3}$$

with M_d the disc mass, r_d and z_0 are the radial scale length and vertical scale thickness respectively. The election of the dark matter halo determines the parameters of the disc embedded within it. Several studies have been developed with objective of determine the parameters for realistic stable discs [Mo 1998]. The values adopted for the disc based on this previous investigations where $r_d = 1.53$ Kpc, $z_0 = 0.31$ Kpc and $M_d = 3.3 \times 10^9{\rm M}_\odot$. The host galaxy, halo and disc, is the same for all simulations.

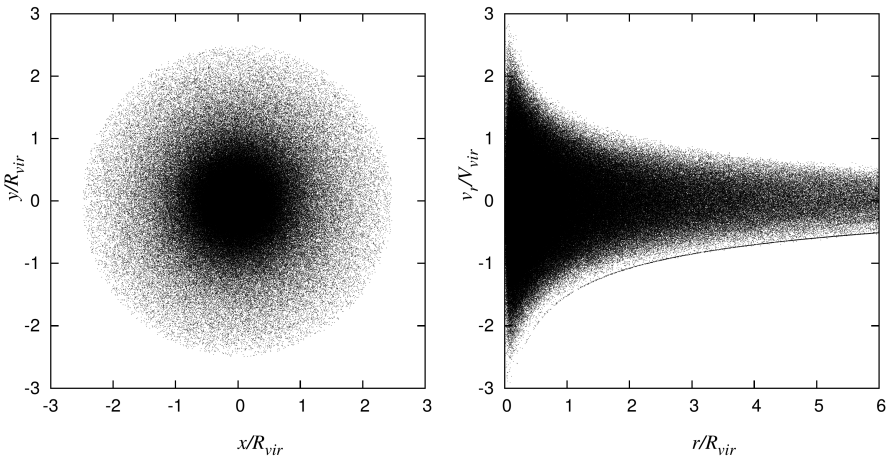

Figure 3.1: *Left panel*: Projected spatial distribution in the $x-y$ plane of a dark matter Henrquist's halo. *Right panel*: Velocity profile in the spherical radial coordinate of the Hernquist's halo. $R_{\rm vir} = 46.44$Kpc, $V_{\rm vir} = 177.64$ Km/s.

3.1.2 The Satellite Galaxy

The satellite galaxy was modelled as an spherical symmetric distribution of particles that follow the Hernquist profile [Hernquist 1993]

$$\rho_{\rm satellite}(r) = \frac{M_s}{2\pi}\frac{a}{r(a+r)^3}, \tag{3.4}$$

where M_s is the satellite mass and a is the satellite scale radial length which corresponds with the Second Most Massive Progenitor in the CLUES simulation used for this work. As it will be explained in the next chapter, the satellite galaxies in the different experiments have the same mass and size, with the

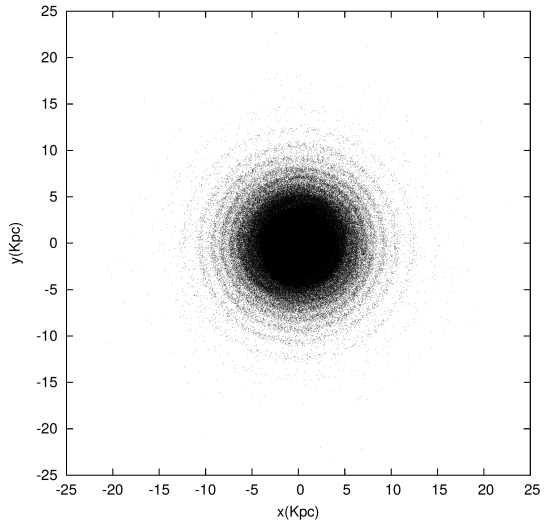

(a)

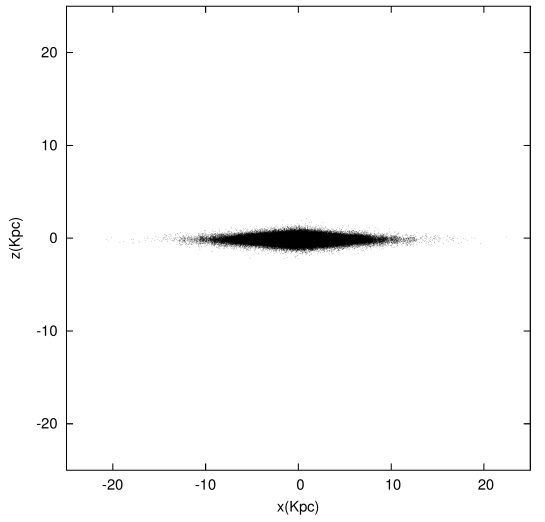

(b)

Figure 3.2: *Upper panel*: Galactic disc seen face on. *Bottom panel*: Galactic disc seen edge on.

variation of other parameters as resolution and orbital configuration. The parameters for the satellite galaxy are $r_{200} = 21.38$ Kpc, $M_s = 2.5 \times 10^{10} \mathrm{M}_{\odot}$ and $c = 4.26$.

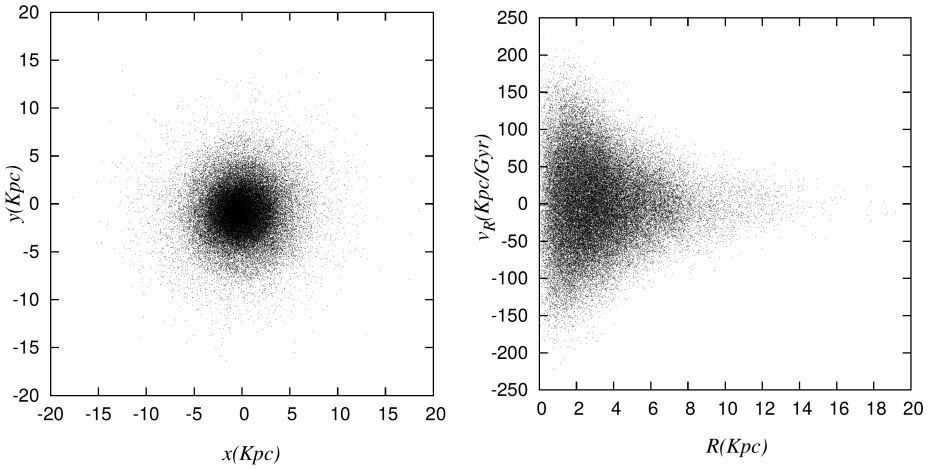

Figure 3.3: *Left panel*: Projected spatial distribution in the $x-y$ plane of a disc planar to the $x-y$ plane. *Right panel*: Velocity profile in the cilindrycal radial coordinate of the exponential disc.

3.1.2.1 Including Gas

The collisional component was included only in the satellite galaxy, since it is in the satellite galaxy where we want to study the evolution of the gas and its effects on the formation of globular cluster candidates. The gas was originated following exactly the same distribution than the satellite galaxy, with the same spatial parameters but with different number of particles.

The mass of the gas was chosen as the 16.6% of the total mass of the satellite galaxy in order to have the maximun amount of gas available permitted by the Λ-CDM model. The merger are therefore *wet* mergers. To generate the gas supplied satellite, we simply attach the pure gaseous satellite described in the previous paragraph to the original pure dark matter satellite, this is, we locate the two distributions in the same spatial location and the two distributions thus form the satellite galaxy.

The gas is in hydrostatic equilibrium inside the satellite gravitational potential with an isotropic temperature profile

$$T(r) = \frac{m_p}{k_B}\frac{1}{\rho(r)}\int_r^\infty \rho(r)\frac{GM(r)}{r^2}\mathrm{d}r, \tag{3.5}$$

where m_p is the proton mass and $M(r)$ is the cumulative total mass and

$\rho(r) = \rho_{\text{satellite}}(r)$ [Mastropietro 2005].

3.2 Numerical Realizations

Using the density profiles expressed in the formulae of the previous paragraphs, we can write the corresponding expressions for number density of each component. Namely, for the host halo

$$n_{\text{halo}} = 2a_h N_h \frac{r}{(r+a_h)^3}, \tag{3.6}$$

is the aforementioned number density with N_h the number of particles of the dark matter halo. For the stellar disc, we have

$$n_{\text{disc}} = \frac{N_d}{2\pi r_d^2 z_0} R\text{sech}^2(z/z_0)\exp(-R/r_d), \tag{3.7}$$

in which N_d is the number of particles of the disc. Given our construction of the satellite and its gaseous component, the number density expression for the stellar and gaseous components of the satellite differs only on the number of particles, like mass density changes only in the total mass of each component. In compact form, this is

$$n_{\text{satellite,gas}} = 2aN_{s,g}\frac{r}{(r+a)^3}, \tag{3.8}$$

where N_s and N_g are the number of particles of stars and gas in the satellite respectively. The ensemble of particles finally distributed according to the distributions shown are obtained using an algorithm of *Acceptance/Rejection*. Roughly speaking, a set of points is randomly generated in a certain region of the space. Then, the point generated is evaluated using the Von Neumman algorithm to accept or reject the point as a realization of the corresponding distribution function.

The generation of velocities was also performed with the *Acceptance/Rejection* technique. To assign velocities to each particle, the moments of the *Collisioneless Boltzmann Equation* are used and the rejection select the correct realization for the corresponding velocity distribution, Maxwellian in the case of the spherical systems and normal for the flattened systems [Hernquist 1993]. Figures 3.1 and 3.4 show the result of the initial conditions generation process for the host dark matter halo and for the pure dark matter satellite. The plots include the velocity profile of both halos. Figure 3.2 is the initial generated disc, seen face-on and edge-on. This plot was done with the disc of higher resolution.

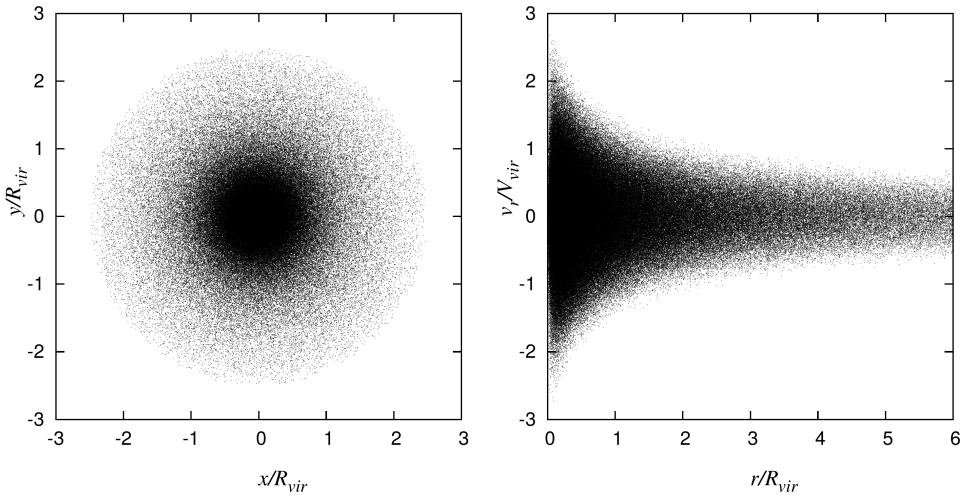

Figure 3.4: *Left Panel* Projected spatial distribution in the $x-y$ plane of a satellite spheroidal satellite galaxy. *Right Panel*: Velocity profile in the spherical radial coordinate of the Herquist's satellite. $R_{\rm vir} = 21.38$Kpc, $V_{\rm vir} = 59.76$ Km/s.

3.3 Initial Positions

The initial position of the host galaxy was chosen as the origin of coordinates and the initial position of the satellite was chosen according to the following procedure. The initial position $\mathbf{r}_0$ and velocity $\mathbf{v}_0$ of the satellite galaxy were chosen by determining the most probable orbital parameters that the subhalos infalling a host halo will have. According to [Wetzel 2011], the circularity η and the pericentre r_p depend on the host halo mass $M_{\rm host}$ and redshift z and are distributed at the moment of their passage through the host's virial radius in the following way

$$\frac{{\rm d}f(M_{\rm host},z)}{{\rm d}\eta} = C_0(M_{\rm host},z)\eta^{1.05}(1-\eta)^{C_1(M_{\rm host},z)}, \tag{3.9}$$

$$\frac{{\rm d}f(M_{\rm host},z)}{{\rm d}r_p} = R_0(M_{\rm host},z)\exp\left\{-[r_p/R_1(M_{\rm host},z)]^{0.85}\right\}. \tag{3.10}$$

	α_i	β_i	γ_i	$g_i(z)$
C_0	3.38	0.567	0.152	1
C_1	0.242	2.36	0.108	1
R_0	3.14	0.152	0.41	$(1+z)^{-4}$
R_1	0.45	-0.395	0.109	$(1+z)^{-4}$

Table 3.1: Parameters for the functional fits of the orbital distributions from [Wetzel 2011]

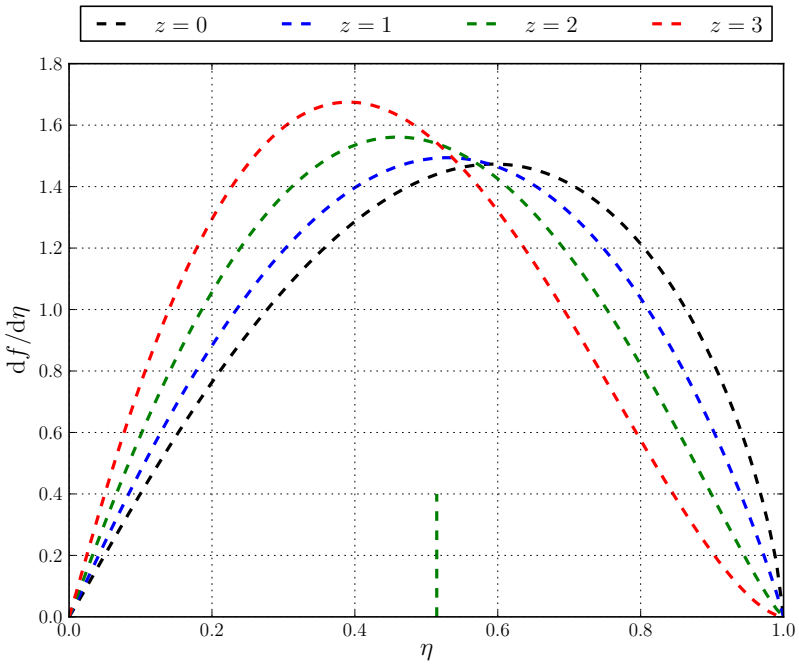

Figure 3.5: Circularity distribution for the infalling satellites. The small vertical line indicates the average for $z = 2$

Where the coefficients $C_i(M_{\rm host}, z)$ and $R_i(M_{\rm host}, z)$, $i = 0, 1$ encapsulate the host halo mass and the redshift dependence that the orbital parameters exhibit. $M_*(z)$ is the characteristic halo mass scale of collapse at z. The coefficientes have the functional form found in [Wetzel 2011]:

$$C_i, R_i = \alpha_i \left(1 + \beta_i \left[g_i(z) \frac{M_{\rm host}}{M_*(z)}\right]^{\gamma_i}\right). \tag{3.11}$$

The parameters α_i, β_i, γ_i are summarized in table 3.1 and $g(z)$ is a function with the explicit dependence on redshift. An usefull approximation to the relation between $M_*(z)$ and z is also given by [Wetzel 2011], namely

$$\log\left[M_*(z)/h^{-1}\mathrm{M}_\odot\right] = 12.42 - 1.56z + 0.038z^2, \tag{3.12}$$

and we use it to calculate the orbital parameters of our satellite galaxy. From table 4.1, the mass of the host is $M_{\rm host} = 4.6\times10^{11}{\rm M}_{\odot}$ at $z = 2$. Then, equation 3.12 allows us to calculate the relation $M_{\rm host}/M_*(z)$ and equations 3.9 and 3.10 determine the distributions of pericenters and circularities at infall for our simulations. Figures 3.5 and 3.6 shows the calculated distributions for our host halo and redshift. Orbit circularity has a nearly constant small rate of decrease with redshift while pericentre distance exhibits a decrease in its average values with z. In particular, at $z = 2$ we obtain an average pericentric distance of $0.27R_{\rm vir}$, with $R_{\rm vir}$ the virial radius of the host halo. For this halo $R_{\rm vir} \approx r_{200} = 63.29$Kpc. The average circularity at $z = 2$ is 0.54. With this two values we calculate the eccentricity e and apocentric distance r_a using the two body approximation as

$$e = \sqrt{1-\eta^2}, \tag{3.13}$$

$$r_a = \left(\frac{1+e}{1-e}\right) r_p. \tag{3.14}$$

For our system the numerical values are $e = 0.84$ and $r_a = 198.34$Kpc. Finally, making use of the *vis-viva* equation, the velocity at apogalacticon is simply

$$v_a = \sqrt{2\frac{GM}{r_a}(1-e)}, \tag{3.15}$$

which is 34.9 Km/s.
Based on the satellite parameters given in the previous paragraph, the merger was disposed in five different configurations. Its main differences are their location relative to the disc plane and its orbital movement direction relative to the disc rotation. The configuration parameters are shown in table 3.2 and a schematic illustration of all of them are represented in figure 3.7

Name	Nomenclature	$\mathbf{r}_0$ (Kpc)	$\mathbf{v}_0$(Km/s)
Perpendicular	*p*	(0,0,198.34)	(0,34.9,0)
Planar Corrotating	*pcr*	(0,198.34,0)	(-34.9,0,0)
Planar Contrarotating	*pct*	(0,198.34,0)	(34.9,0,0)
Inclined Corrotating	*icr*	(99.6,99.6,140.25)	(-24.67,24.67,0)
Inclined Contrarotating	*ict*	(99.6,99.6,140.25)	(24.67,-24.67,0)

Table 3.2: Simulations' orbital configurations

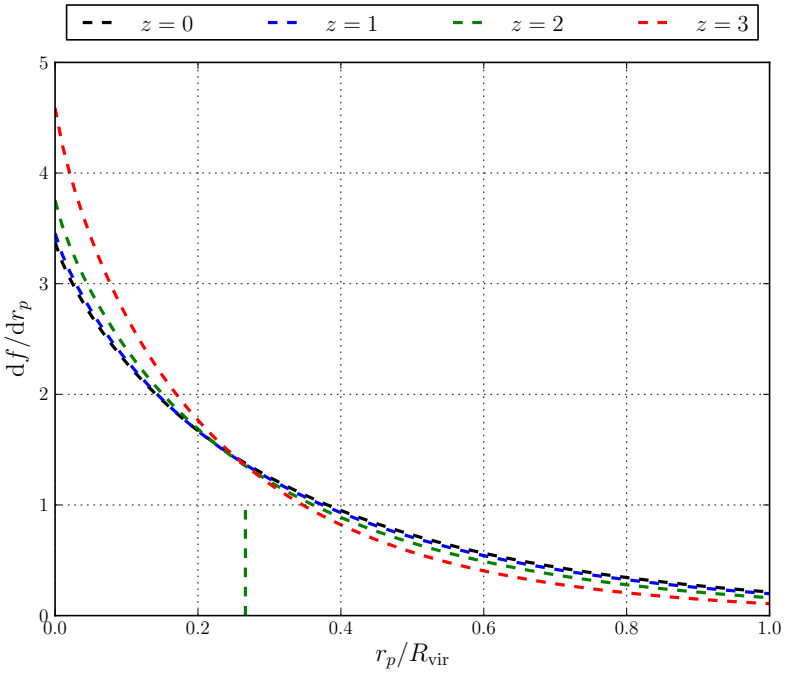

Figure 3.6: Pericentre distribution for the infalling satellites, redshift dependence is explicitly noted. The small vertical line indicates the avarage value for $z = 2$.

3.4 Gravitational Potential Evaluation

As a first approximation tool to explore the possible substructures in the stream at the output of the simulations, we use the gravitational potential over a star belonging to the stream, due only to the rest of stars in the stellar stream. The first issue here is to distinguish between the particles that actually belong to the stream and those that remain bound to the satellite. This procedure will be exposed in detail in section 4.1.1; here we just show the main goal to perform such calculation.

The potential over the star j generated by the distribution of particles of the stream is calculated by

$$\Phi^{j}_{\mathrm{Stream}} = -G \sum_{i \neq j}^{N_{\mathrm{Stream}}} \frac{m_i}{r_{ij}}, \tag{3.16}$$

where N_{Stream} is the number of particles of the stream in every snapshot. This potential was calculated using a tree code, described below.

The tree algorithm begin constructing a cubic cell containing the entire system of particles, which is the root node. If the node has more than one particle, the cell is divided into eight identical cubic cell, called daughter cells. This procedure is recursively performed until all the daughter resulting cells have exactly one particle

regardless several cell could, in fact, be empty.

The potential evaluation of a given particle is carried out recursively depending on the open tolerance θ. If l is the size of the cell under consideration and D is the distance from the cell center of mass to the particle then, if $l/D > \theta$ the cell is subdivided into eight cells and each one of them is examined again, repeating the division until all the particles have been included. The potential is calculated directly, through 3.16. Otherwise, if $l/D > \theta$, the contribution to the potential of this whole cell is estimated as the potential generated by a pseudo-particle. To increase the accuracy of this approximation, the potential of the particle distribution in the cell is estimated using the multipole gravitational moments of the distribution, usually until the quadropole term

$$\Phi(r) = -G\left(\frac{M}{r} + \frac{Q_{ij}r_i r_j}{2r^5}\right), \tag{3.17}$$

where the repeated indices are summed from 1 to 3. The position vector $\mathbf{r}$ is expressed with respect to the center of mass of particles in the cell. The monopole M and the quadrupole Q are

$$M = \sum m_k, \tag{3.18}$$

$$Q_{ij} = \sum m_k(3x_{i,k}x_{j,k} - |\mathbf{x}_k|^2\delta_{ij}). \tag{3.19}$$

The dipole term vanishes since $\mathbf{r}$ is expressed relative to the center of mass of the distribution [Aaerseth 2003].

The calculation is performed in every snapshot. The gravitational potential is plotted in figure 3.8 for the radial coordinate with the clump in the potential stream still visible.

3.5 Density Computation

The best way to identify substructure that could potentially be associated to a globular cluster in our simulations is through the computation of the spatial mass density of stars in the body of the stellar stream [Diemand 2008]. We evaluate the density of the discrete set of points using the *EnBiD*(Entropy Based Binary Decomposition) algorithm [Sharma 2006]. In this algorithm, the tesselation of the space is performed estimating the *Shannon Entropy* for each dimension, namely

$$S = -\sum_{i=1}^{N_b} p_i \log p_i, \tag{3.20}$$

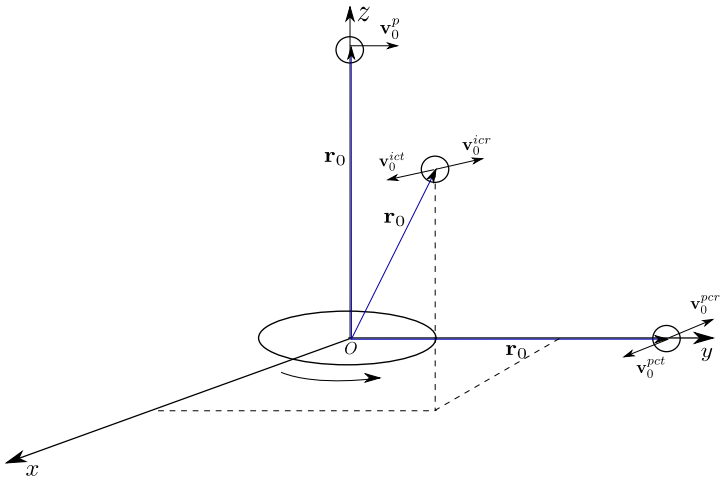

Figure 3.7: Schematic representation for all the initial configurations of the simulations specified in table

with p_i being the probability that a particle is in the ith bin of the equal sized bins in which each dimension is divided. N_b is the number of bins and n_i is the number of particles within the ith bin. Minimum entropy guarantees maximum density variation in that dimension, allowing better recognition of clustered structures within the global distribution of particles. The probability p_i is therefore equal to n_i/N since N is the total number of particles. The dimension that will have minimum entropy will be selected to be splited by a hyperplane perpendicular to it, leaving half of the particles in each resulting subspace. The position of the hyperplane will correspond to the median of the points in the dimension. The process is repeated recursively until each subspace contains only one particle.
To not understimate the densities at the boundary of the subspace due to irregular distribution of the particles within the subspace, the algorithm performs a boundary redefinition of the subspace boundary in order to avoid that the irregular distribution affects the density estimation given that for a particle near the boundary, the nearest neighbors could be truncated by the boundary. Let the maximum and minimum coordinates of a subspace be $l_{\max}$ and $l_{\min}$ in a given dimension. Namely, boundary correction is:

$$l_{\max} \rightarrow x_{\max} + \frac{x_{\max} - x_{\min}}{n_b - 1}, \tag{3.21}$$

$$l_{\min} \rightarrow x_{\min} - \frac{x_{\max} - x_{\min}}{n_b - 1}, \tag{3.22}$$

with n_b being a threshold of particles greater than 7, $x_{\max}$ and $x_{\min}$ the corresponding maximum and minimum coordinates of the particles inside the subspace. The correction is applied when if applied if simultaneously

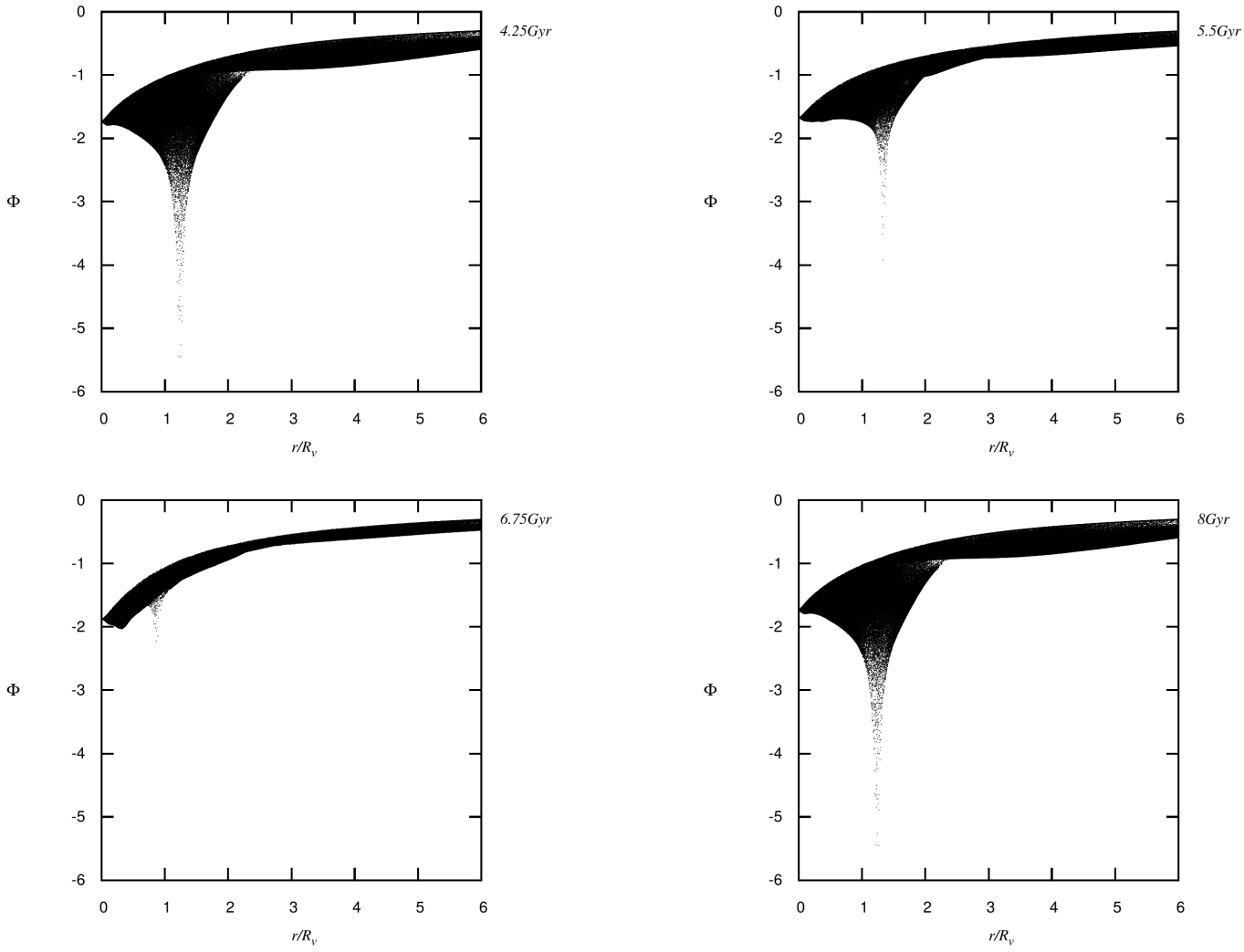

Figure 3.8: Potential projection in the radial direction for the satellite without gas. Φ has units of UnitEnergy/$10^{10}\mathrm{M}_{\odot} \times 10^3$

$$l_{\max} - x_{\max} > f_b \frac{x_{\max} - x\min}{n_b - 1}, \tag{3.23}$$

$$x_{\min} - l_{\min} > f_b \frac{x_{\max} - x_{\min}}{n_b - 1}, \tag{3.24}$$

where f_b is a constant factor related to the number of dimensions of the space d through $f_b = 2N^{1/d}$.

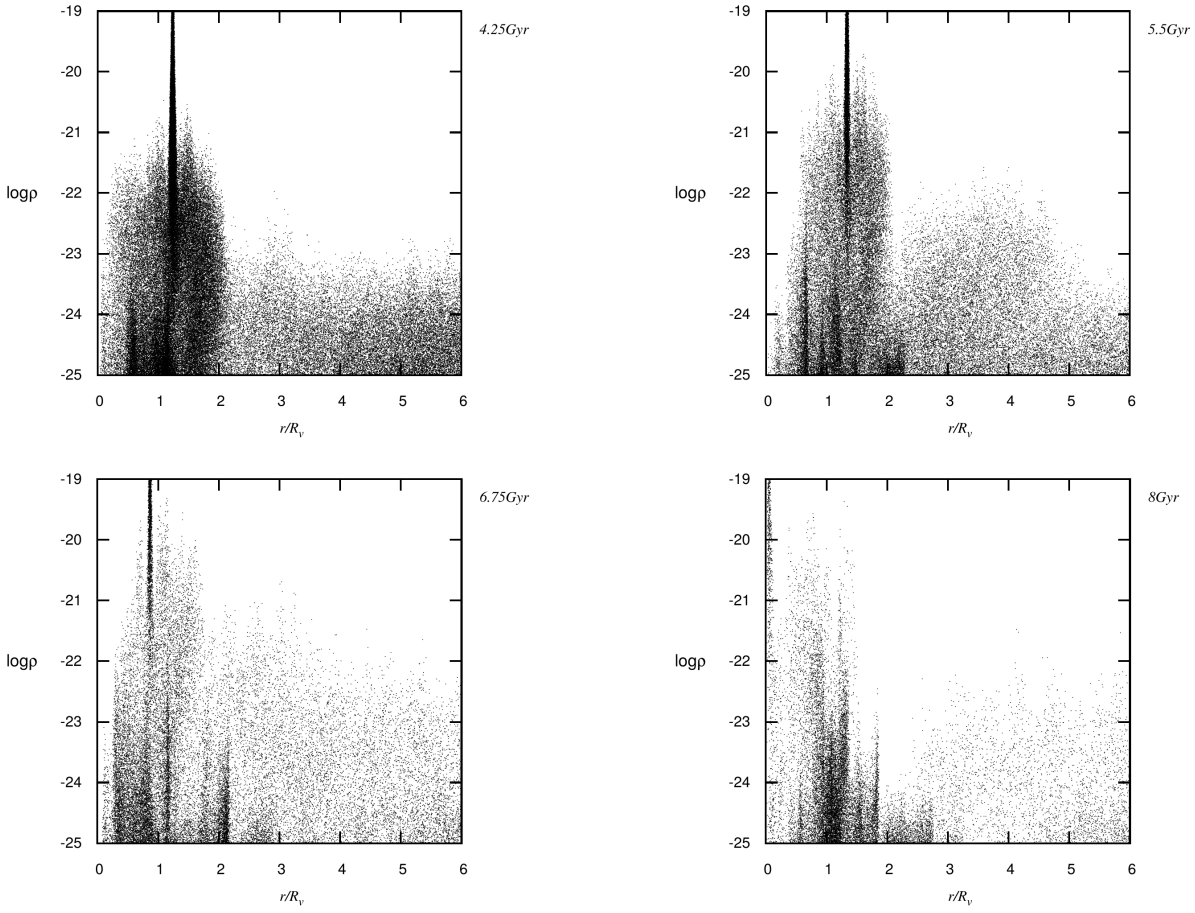

Figure 3.9: Satellite density projected in the radial coordinate. ρ is in $10^{10}\mathrm{M}_\odot/\mathrm{Kpc}^3$

Finally, the density estimation for this work was calculated using the kernel smoothing technique, selecting a fixed number of nearest neighbours around the particle of interest. The kernel could be of two types: Isotropic or Anisotropic. For the isotropic case, the kernel density at a point $\mathbf{x}$ is given by

$$\rho(\mathbf{x}) = \sum_{i}^{n_{\mathrm{ngb}}} m_i W(\mathbf{x}_i - \mathbf{x}, h). \tag{3.25}$$

In different tests, the Epanechikov spherical symmetric kernel gives the better results [Sharma 2006]:

$$W(u) = \begin{cases} (1-u^2) & 0 \leq u \leq 1 \\ 0 & \text{otherwise} \end{cases}, \quad u = \sqrt{\sum_{j=1}^{d} \left(\frac{x_j}{h_j}\right)^2}. \tag{3.26}$$

The smoothing parameter $\mathbf{h}$ is chosen such that it encloses the fixed number of neighbours n_{ngb}, thus varying in space and time in order to reflect the variations of the local interparticle separation.
The spherical kernel is finally written as a product one-dimensional kernels as

$$W(\mathbf{x}, \mathbf{h}) = \frac{f_d W_d(u)}{\prod_{i=1}^{d} h_i}, \tag{3.27}$$

where f_d is a normalization constant given by

$$f_d = \left(\int_0^1 W(u) S_d u^{d-1} \mathrm{d}u \right)^{-1}, \tag{3.28}$$

the computation involves the surface of a unit hypersphere in d-dimensions, namely:

$$S_d = \frac{2\pi^{d/2}}{\Gamma(d/2)}, \tag{3.29}$$

where Γ is the Delta function.
The smoothing length defines a region of influence for each particle. This region is then a sphere of radius $l \times h$, with $2 \leq l \leq 3$ containing the nearest neighbours, that is, the kernel is isotropic. As the surroundings of each particle change in space and time, the value of h also vary for each particle and for different times, in such a way that the number of neighbors remain the same. In some situations, the heighbours of a given particle could agglomerate along certain direction, causing the isotropic kernel to understimate the density of the particle. Anisotropic kernels are build to adapt to those anisotropic clumps of particles, reflecting the different interparticle separation in the vecinity of the particle along different directions. This approach defines an ellipsoid around each particle instead of a spherical region as in the isotropic case. The ellipsoid built to take into account the anisotropy of the particle distribution. The anisotropic formalism made use of the *anisotropic smoothing tensor* $\mathbf{H}$ to define the axes of the the triaxial ellipsoid around a particle i.

$$\mathbf{H} = \begin{bmatrix} h_{1x} & h_{2x} & h_{3x} \\ h_{1y} & h_{2y} & h_{3y} \\ h_{1x} & h_{2z} & h_{3z} \end{bmatrix}, \tag{3.30}$$

with each column defining one of the three axis vector $\mathbf{h}_k$. The ellipsoid defined by $\mathbf{h}_k$ accommodates according to the instantaneous motion of the fluid around a particle located at the point $\mathbf{x}$. In general terms, the motion is characterized by

the velocity $\mathbf{v}(\mathbf{x}, t)$ and the different spatial rates of change in those velocities is accounted in the deformation tensor

$$\sigma_{ij} = \frac{1}{2}\left(\frac{\partial v_i}{\partial x_j} + \frac{\partial v_j}{\partial x_i}\right). \tag{3.31}$$

If the length of the k, $(k = 1, 2, 3)$ axis of the ellipsoid at time t is $h_k(t)$, the value of this length will change to a value of $h_k(t + \delta t)$ due to contractions or dilations during the interval δt. If λ_k are the eigenvalues of σ_{ij}, the length of the axis at $t+\delta t$ is given by:

$$h_k(t + \delta t) = h_k(t)(1 + \lambda_k \delta t). \tag{3.32}$$

The initial values of the axis lengths are chosen to be the smoothing length of the isotropic kernel defining a sphere of influence for each particle, and then, each length evolves in the way described previously. The anisotropic kernel is written as [Sharma 2006]:

$$W(\mathbf{x}, h) = \frac{f_d}{|\mathbf{D}|^{1/2}|\mathbf{H}|} W(|\mathbf{D}^{1/2}\mathbf{E}\mathbf{H}^{-1}\mathbf{x}|). \tag{3.33}$$

Where $\mathbf{E}$ is the eigenvalue matrix that diagonalizes the covariance matrix $\mathbf{C}$ at the point $\mathbf{x}' = \mathbf{H}^{-1}\mathbf{x}$ and $\mathbf{D}$ is the corresponding diagonal eigenvalue matrix.

Chapter 4

Streams, Clusters and Substructures of the Satellite Galaxies

Contents

4.1 Simulations without Gas 39
4.1.1 Identification Of Streams 40
4.1.2 Stream Substructures 44
4.2 Simulations with Gas 47
4.2.1 SPH Artificial Fragmentation 48
4.2.2 Globular Clusters Candidates 49
4.2.3 Analysis and Conclusions 52

In order to evaluate the possibility of formation of globular clusters from the material striped during a minor merger, we performed in the first instance, simulations without the collisional component, i.e. simulations with satellite galaxies totally devoid of gas. In this chapter the design of such simulations, their properties and the main results of this experiment are described.
In the second part of this chapter we describe the simulations performed with gas, star formation and cooling in the satellite galaxy and the subsequent analysis done on them in order to identify gas clouds that potentially host progenitors of globular clusters and present the results of these analyzes.

4.1 Simulations without Gas

The main purpose of these experiments consists in verify if a pure collisionless stream could contain particles that eventually cluster and form some bound system, without the influence of gas. We performed two sets of simulations, varying the resolution of the experiment, this is, for the same satellite galaxy the total mass remains constant, but the number of constituents particles was duplicated. The total masses, number of particles and mass per particle are summarized in tables 4.1 and 4.2

	Mass ($M_\odot$)	Number of particles	Mass per particle ($M_\odot$)
Satellite	3.2×10^{10}	1×10^5	3.2×10^5
Disc	3.3×10^9	5.6×10^4	6×10^4
Halo	7.9×10^{11}	7.3×10^5	1.1×10^6

Table 4.1: Masses and number of particles for the satellite halo and each component of the host galaxy for the lowest resolution simulation without gas.

The analysis starts with the identification of the stream of material stripped out from the satellite during the merger, then we calculate the potential and the density using the methods shown in the previous chapter to identify any structure that could be formed during the interaction. These structures may provide hints on the places where gas can collapse, form stars and globular clusters.

	Mass ($M_\odot$)	Number of particles	Mass per particle ($M_\odot$)
Satellite	3.2×10^{10}	2×10^5	1.6×10^5
Disc	3.3×10^9	5.6×10^4	6×10^4
Halo	7.9×10^{11}	7.3×10^5	1.1×10^6

Table 4.2: Masses and number of particles for the satellite halo and each component of the host galaxy for the highest resolution simulation without gas.

In total we ran ten collisionless simulations, two for each orbital configuration defined in table 3.2. The first set of simulations consisted in one run from each configuration with number of particles specified in table 4.1 while the second set used the values in table 4.2. The reason of simulate the same simulation with two different satellite number of particles was to evaluate the impact of resolution in the behavior of the particles in the merger, for instance, to study if the possible potential wells of the potential cluster progenitor change in deep with resolution.

4.1.1 Identification Of Streams

We define the tidal stream as composed by the particles that have escaped from the gravitational influence of the satellite galaxy. In other words, it is made of particles who became unbound from its original host potential and pass to orbit the main galaxy potential. To identify the stream's particles, we proceeded as follows:

- In the initial configuration, $t = 0$ we calculate the position and velocity of the center of mass of the satellite respect to the origin of coordinates. If $\mathbf{r}_i$ and $\mathbf{v}_i$

are the position and velocity of a particle of mass m_i, for the center of mass:

$$\mathbf{r}_{\rm cm} = \frac{1}{M}\sum_{i}^{N} m_i \mathbf{r}_i, \tag{4.1}$$

$$\mathbf{v}_{\rm cm} = \frac{1}{M}\sum_{i}^{N} m_i \mathbf{v}_i, \tag{4.2}$$

where M is the total mass of the satellite.

- In order to calculate the mechanical energy E_i of each particle at this initial time respect the center of mass of the satellite, we translate the center of coordinates to the center of mass recently calculated by the simple transformations of positions $\mathbf{r}'_i = \mathbf{r}_i - \mathbf{r}_{\rm cm}$ and velocities $\mathbf{v}'_i = \mathbf{v}_i - \mathbf{v}_{\rm cm}$. Therefore, the mechanical energy of each particle respect to the center of mass of the satellite is

$$E_i = \frac{1}{2} m_i v_i'^2 - G\sum_{i<j}^{N} \frac{m_i m_j}{r'_{ij}}, \tag{4.3}$$

where $r'_{ij} = |\mathbf{r}'_j - \mathbf{r}'_i|$.

- The set of particles having the lowest energies are stored in a new set, named the more bounded particles. The number of particles of this more bounded set is arbitrary fixed but we assume at this point that this initial set of more bounded particles remains as the more bounded particles to the satellite across the entire simulation.

- At each timestep of the simulation, we track the more bounded particles identified at $t = 0$ and compute the center of mass for them. This center of mass is assumed to be the center of mass of the satellite itself, since it has been assumed that this more bound particles remain being the most bound particles of the satellite galaxy throughout the simulation. This can be verified in figure 4.1 showing that indeed, assuming that the set of most bounded particles can be used to track the movement of the satellite during the simulation. As a first step to verify the operation of the stream identification procedure, we track the center of mass of the satellite for each simulation checking that indeed the center of mass follows a smooth orbit that spirals toward the galactic disk.

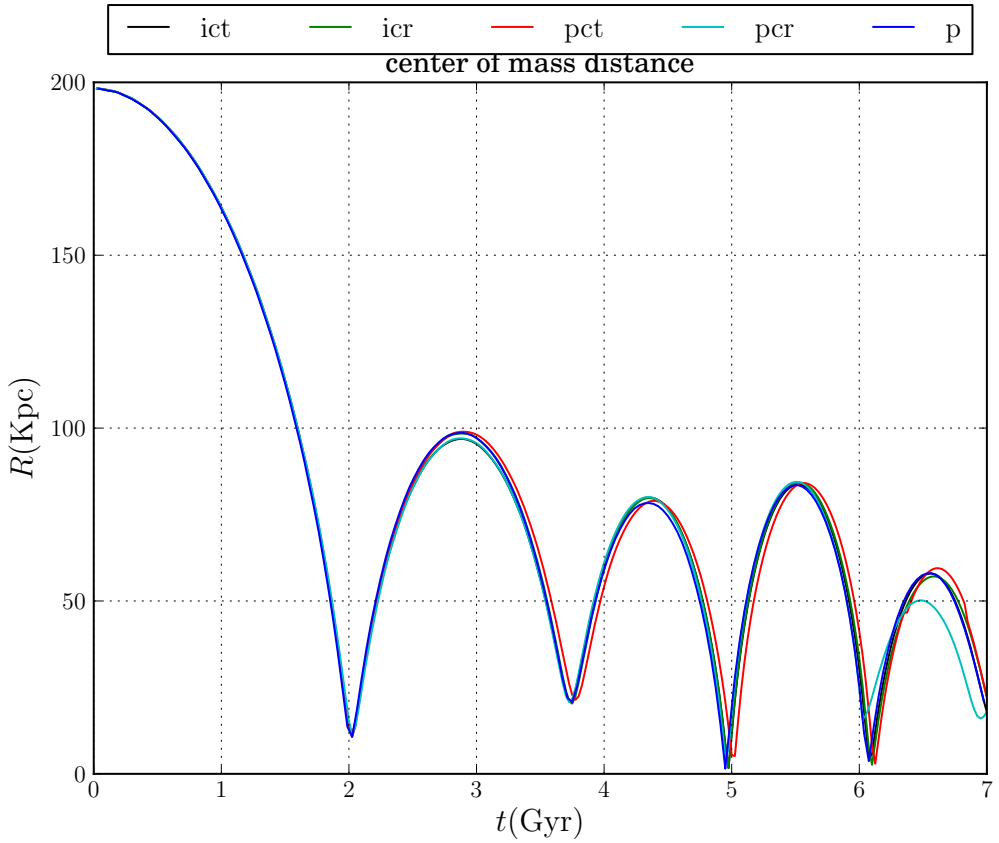

Figure 4.1: Evolution of the radial distance of the satellite center of mass in time for each orbital configuration.

- Once the position and velocity of the center of mass of the galaxy for each timestep are determined, the mechanical energy of each particle is recalculated relative to the new center of mass by means of 4.3.

- With a definite value of the binding energy, the stars are then segregated into those who still belongs to the satellite galaxy ($E_i < 0$) and those who are not bounded anymore to it ($E_i > 0$). The last ones are said to be part of the tidal stream.

The separation scheme allows a clear identification of structure formed by the particles stripped away from the satellite galaxy. In figure 4.2 it is shown the projected positions on the $z - y$ plane of the stellar stream and the satellite galaxy separated with the previous criterion at different times of the merger with the host galaxy. Tidal features known as umbrellas can be clearly appreciated in the late phase of the stream evolution when the satellite galaxy is almost fully disrupted.

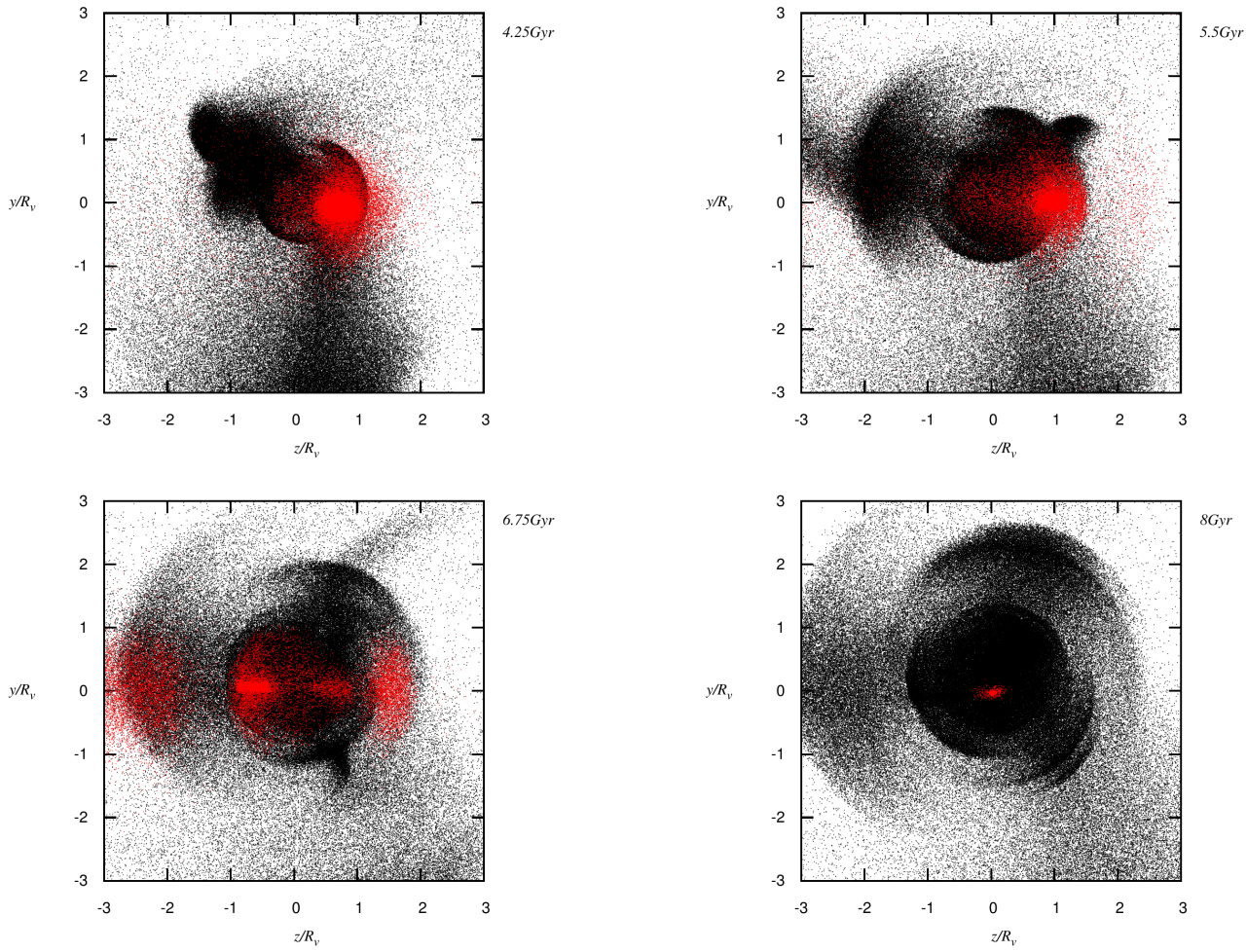

Figure 4.2: Satellite (red) and Stream (black) projected positions on the $z-y$ plane for 4.25, 5.5, 6.75 and 8.0 Gyr

From our simulations it can be seen that the tidal forces tear apart increasingly particles of the satellite, greatly increasing the spatial extent and mass of the stream. Figure 4.3 shows the rate of mass gain/loss for the stream/satellite in the different satellite orbits. The orbital configuration is not important until the first perigalacticon passage at $t \approx 2$ (compare with figure 4.1), thereafter, the mass loss is more significant for the satellite whose orbit is in the same direction of rotation of the disk, indicating that tidal shocks by the disk are stronger in this situation, which

was expected since the transference of momentum is greater in this configurations where the angular momentum of the disk and the orbital momentum of the satellite are in resonance [Binney 2008].

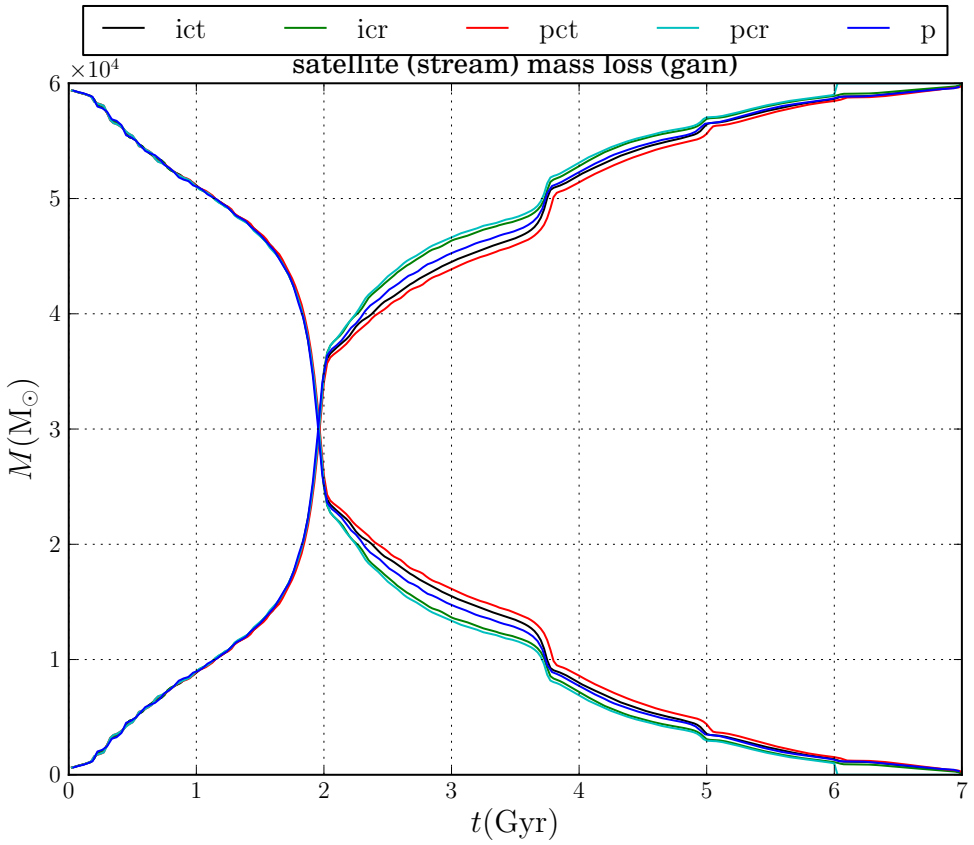

Figure 4.3: Comparative mass gain/loss by the stream/satellite for all initial orbital configurations of the satellite. Relative rotation to the disc become important after the first passage through the galactic disc. Disc shock are more pronounced in corrotating configurations.

4.1.2 Stream Substructures

The particles of the stream can eventually experience some perturbation or instability that could bound nearby particles in a new stellar subsystem. Depending on the stability of this new born structure, it could evolve to an autonomous structure independent of the satellite. There are several types of stellar structure that the new stellar system could form, as spikes or umbrellas (see figure 4.2), but the aim of this work is evaluate the probability that the new system is, indeed, a globular cluster.

As a substructure forms inside a tidal stream, the particles that now belong to the new born stellar system will be located in the same region of space further shar-

ing similar velocities respect to some observer increasing the density in both the configuration and phase spaces.

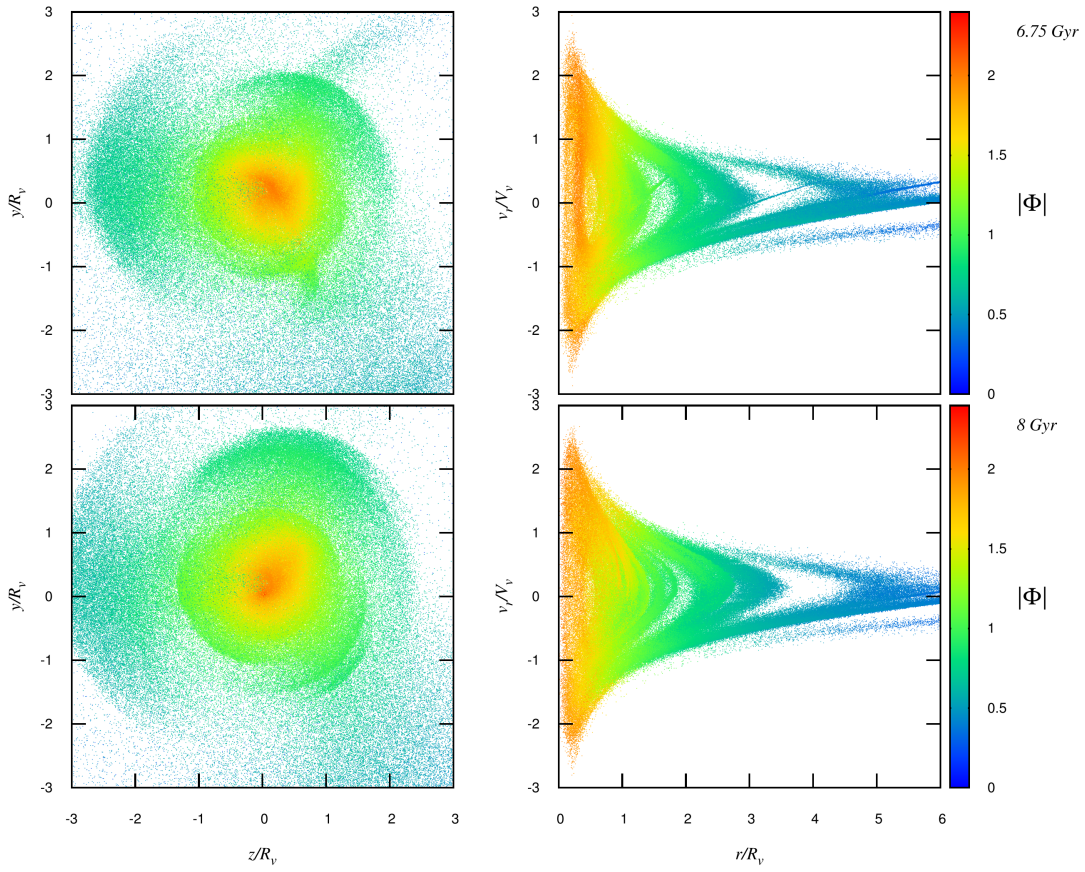

Figure 4.4: *Left Panel:* Real space projection on the $z-y$ mapped with the potential intensity. *Right Panel:* Phase space projection on the $r - v_r$ plane with same potential color mapping. There is not decentralized potential wells in which a bound structure could develop.

Substructures embedded in the distribution of stream particles then manifest as overdensities in both spaces. If the substructure is large enough, the potential well of the overdensity would become deeper than the potential of the stream. In first instance we proceeded looking for the potential wells in the stream particles generated by the clustering of stars. Figure 4.4 summarizes the results of this task. Distances and velocities are measured from the center of the satellite for

figures 4.4 and 4.5. Color mapping allows to establish that caustic regions are under approximately the same potential, which is expected for an umbrella-like structure since its particles are at similar distance from the center of the satellite galaxy.

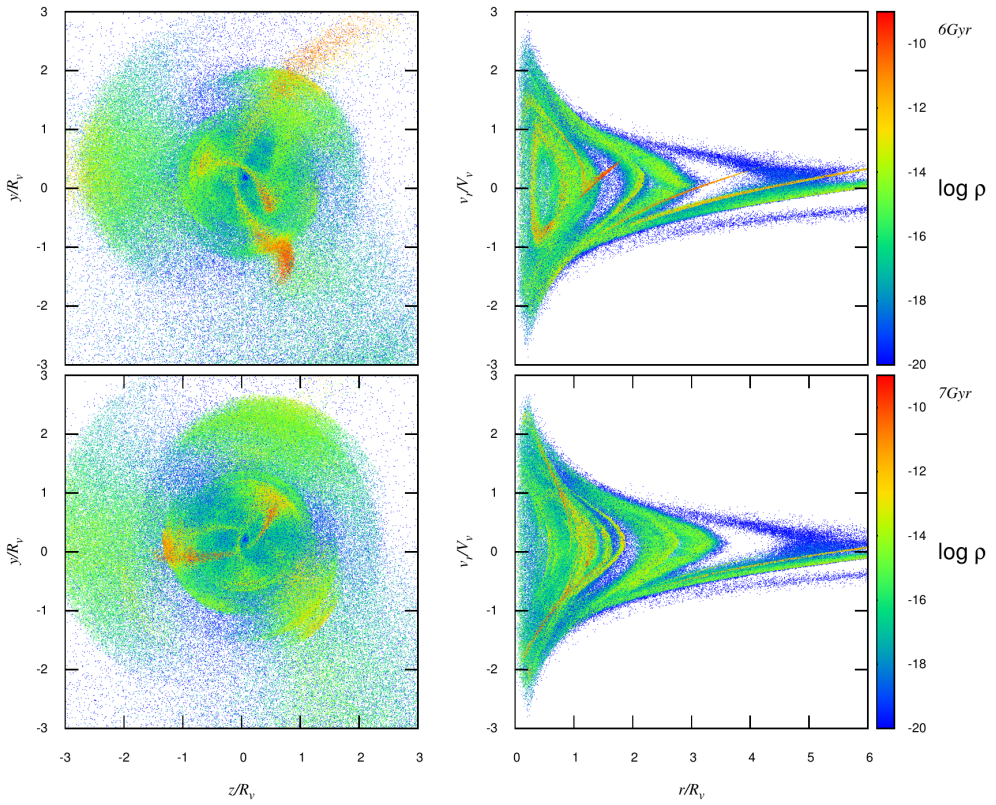

Figure 4.5: *Left Panel:* Real space projection on the $z - y$ mapped with density. *Right Panel:* Phase space projection on the $r - v_r$ plane with same density color mapping. The density contrast is specially high in the tidal sparks, but still do not exhibit the morphology of a globular cluster.

The color map does not highlight any regions, apart from the central region, in which the clustering of particles produce a deeper potential well than its surroundings, that is because the clumps do not have a deep enough potential to stand out over the stream potential. This conclusion does not rule out the possibility that particle associations can actually be bounded structures.
The estimation of the potential in the stream to identify the clumps proved to

be inconclusive. Density maps, conversely, clearly shows the regions in which the spatial density is significantly high relative to the stream density. However, these high density structures did not exhibit a morphology or a velocity dispersion pattern similar to those of a globular cluster, as can be seen in figure 4.5. The structures were not remained for significant periods of time, leading us to conclude that, in absence of collisional matter, the formation of a cluster-like structure has a very low probability to form.
Structures arising in the collisional simulations are not stable in the sense that their morphology changes dramatically over time and disappear relatively quickly. However, the structures formed are regions of high density in which gas could cool and collapse, thus catalyzing the formation of globular clusters.

4.2 Simulations with Gas

In last section we showed that in non-dissipative simulations it could be possible to form transient structures but they do not live longer enough to be called clusters. However they can provide the potential well where gas can cool and condense to form deeper potential wells and form a bound system. These set of simulations depict a more realistic scenario by adding gas particles to the satellite galaxy. Basically, the initial configurations of the simulations with gas were exactly the same as those without gas, that is, equal masses for the host and the satellite galaxy and the same initial orbital configuration. The gas in the satellite was added as a spheroidal distribution according with 3.4 whose mass was taken as the 16.6% of the total mass of the satellite, totaling a mass of $3 \times 10^{10} M_{\odot}$ for the satellite galaxy.

	Mass ($M_{\odot}$)	Number of particles	Mass per particle ($M_{\odot}$)
Gas	5×10^9	2×10^4	2.5×10^4
Satellite	2.5×10^{10}	4×10^4	6.2×10^4
Disc	3.5×10^9	5.6×10^4	6.4×10^4
Halo	7.9×10^{11}	7.3×10^5	1.6×10^6

Table 4.3: Total masses and particle numbers of the different components in the simulations with gas. This simulation corresponds to the lowest resolution of the set of the three simulation with a satellite galaxy with gaseous content or HR1.

The simulations run include dissipative effects as star formation, radiative cooling and supernovae feedback with SPH parameters of maximum number of neighbors and temperature set to 28 and 1000 K respectively. In this way we incorporate the main physical processes to evaluate the formation of clusters within the tidal streams.

4.2.1 SPH Artificial Fragmentation

The numerical scheme used to simulate the hydrodynamics of the gas could impact the formation of clumps within the molecular clouds in an artificial way. The resolution of a SPH simulation involving gravity is therefore a critical quantity in order to obtain realistic results from physical process rather than artificially induced mechanisms by numerical fluctuations.
For SPH particles, the smoothing lengths h are constrained to contain approximately a number of particles $N_{\rm ngb}$ in a sphere of radius h, since the gravitational softening is set equal to h, the mass contained in the sphere can not be roughly equal to the local Jeans mass, otherwise the collapse is inhibited by the softening of the gravitational forces.

	Mass ($M_\odot$)	Number of particles	Mass per particle ($M_\odot$)
Gas	5×10^9	4×10^5	1.25×10^3
Satellite	2.5×10^{10}	8×10^5	3.1×10^4
Disc	3.5×10^9	5.6×10^4	6.4×10^4
Halo	7.9×10^{11}	7.3×10^5	1.6×10^6

Table 4.4: Total masses and particle numbers of the different components in the simulations with gas. This simulation corresponds to the medium resolution of the set of the three simulation with a satellite galaxy with gaseous content or HR2.

Thus, the called *minimum resolvable mass*, $M_{\rm res}$ must always be less than the local Jeans mass 2.12. Taking $M_{\rm res}$ as the mass of $2N_{\rm ngb}$ particles, it can be estimated as [Bate 1997]

$$M_{\rm res} = M_{\rm gas}\left(\frac{2N_{\rm ngb}}{N_{\rm gas}}\right), \tag{4.4}$$

where $M_{\rm gas}$ and $N_{\rm gas}$ are the total mass and particle number of the gas. The previous expression explicitly shows that for a larger number of particles, the minimum resolvable mass decreases and the collapse and fragmentation will be less affected for the numerical implementation.
In order to take into account these artificial clustering effects induced by SPH we have therefore performed various simulations, with exactly the same orbital configuration of the pure collisionless simulations and also equal masses but with significant increase in resolution. Tables 4.3, 4.4 and 4.5 contain all the information about the masses and the resolutions of the collisional simulations performed.
The three experiments were run with $N_{\rm ngb} = 128$ for all the simulations. The condition 4.4 is tested for the clumps in the satellite galaxy gas that we selected as globular cluster potential progenitors. The strategy adopted for the identification of the progenitors and the results obtained of such strategy are depicted in the next two sections. Hydrodynamic simulations have much greater computational cost than pure collisionalless simulations, hence we ran one of the possible 5 initial configu-

rations, the referred in table 3.2 as p or perpendicular to the plane disc given that is one of which is experiencing greater mass loss (see figure 4.3). For this unique orbital configuration we then change the resolution of the experiment, the lowest resolution simulation is called HR1 for high resolution first experiment. With the increasing resolution we have HR2 and finally, the highest resolution simulation of this work is called HR3.

	Mass ($M_\odot$)	Number of particles	Mass per particle ($M_\odot$)
Gas	5×10^9	1×10^6	5.0×10^3
Satellite	2.5×10^{10}	3×10^6	8.3×10^3
Disc	3.5×10^9	5.0×10^5	7×10^3
Halo	7.9×10^{11}	1×10^7	7.9×10^4

Table 4.5: Total masses and particle numbers of the different components in the simulations with gas. This simulation corresponds to the highest resolution of the set of the three simulation with a satellite galaxy with gaseous content or HR3.

4.2.2 Globular Clusters Candidates

The possible progenitors for the clusters were selected basically from the phase space density maps. As we have concluded in section 4.1.2, the density maps can highlight the clumps in real space from the phase space estimation of density. The density maps for the gas in the satellite are shown in figure 4.6. Figure 4.8 is simply an agmentation of figure 4.6 to appreciate the clumps in more detail.
Contrary to what happened in the pure collisionless simulations, the gas is clearly clustered in regions with high density which apparently persist for a considerable amount of time. Those clumps in the satellite gas are the primary candidates to form star clusters. The candidates were extracted for the distribution of particles through their high density contrast, following the strategy described below

- First the candidates are identified by performing a selection of particles through a phase space density threshold ρ_{th}. Particles with phase-space densities below the density threshold are definitely ruled out as potentially belonging to some candidate clump. The value of ρ_{th} was chosen examining the values of the density of the simulation using, for instance, a plot of the type of figure 4.7 in which we clearly distinguish between particles of high and low density. In particular, in figure 4.7 we have the density of gas particles accommodated in the interval 0 to 254835 at the x axis, halo dark matter particles in the interval 254836 to 986212, disk particles ranged from 986213 to 1042222, satellite particles go from 1042223 to 1842222 and new stars formed in the gas comprising the interval between 1842223 to 2222800.

- With the candidates identified, for each one of them, we determine the center of the distribution of particles in a particular snapshot of the simulation.

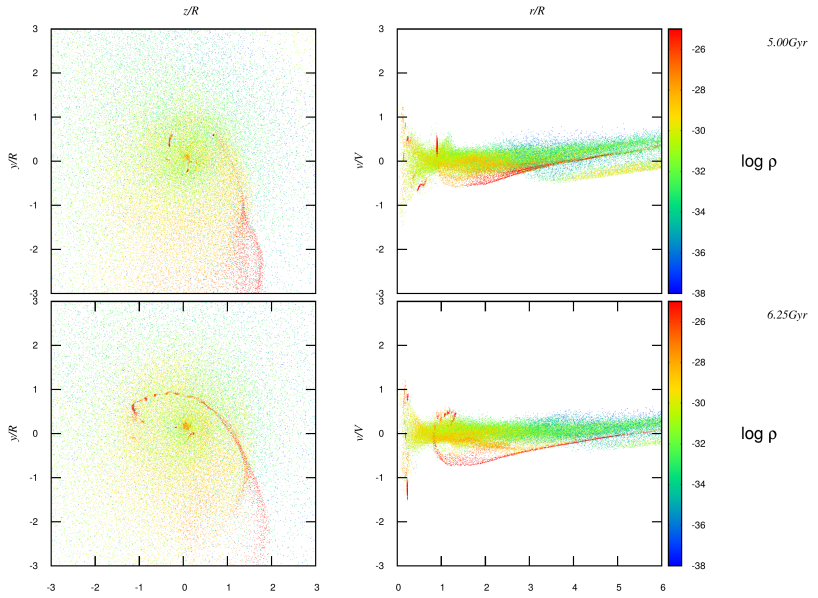

Figure 4.6: *Left Panel:* Real space projection on the $z - y$ mapped with density. *Right Panel:* Phase space projection on the $r - v_r$ plane with same density color mapping. R and V are the virial radius and velocity respectively. Can clearly be seen in the plot the clumps of high density with spheroidal morphologies that seem to orbit the center of the galaxy. This corresponds to a couple of snapshots of HR2. Density units are $10^{10}\mathrm{M}_{\odot}/\mathrm{Kpc}^3$

- Then, gas particles that are within a sphere of a reasonable radius R_0, centered in the center determined in the previous step were selected to track the candidate along the simulation.

- With the identification number of each particle in candidate, we track the position and velocities of that particles in the snapshots preceding and following the one in which the identification was made. In this point, we look for particles of any kind that lie within a sphere or radius R_{th} that time, including dark matter particles from the host and the satellite haloes, disk particles or new stars born during the interaction.

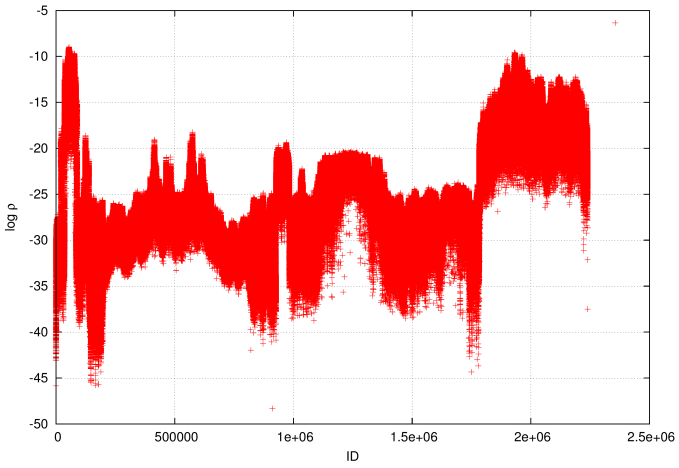

Figure 4.7: Density values for the particles in HR2 $p-$simulation against the identification particle number. This plot correspond to the snapshot at 3.75 Gyr after simulation start. Density units are $10^{10}\mathrm{M}_{\odot}/\mathrm{Kpc}^3$

- For every snapshot, we compute the properties of the clump in order to compare the evolution of the visually identified gas clouds with an astrophysical observed system.

The strategy for the identification of the clumps was applied to the three simulations with the same density threshold. Increasing the resolution results in increasing the density, which is evidenced by a larger number of clumps with high density contrast exhibiting some degree of structure. Figure 4.9 is a comparison of the three simulations at the same simulation time. The number of candidates identified is clearly larger for the high resolution simulation but the relevant fact is that some candidates appear in similar locations in the three simulations, indicating that the formation of this candidates is not due to numerical fluctuations. In the same figure it is also visible structures scattered through space, corresponding to tidally disrupted candidates at this stage of the simulations.

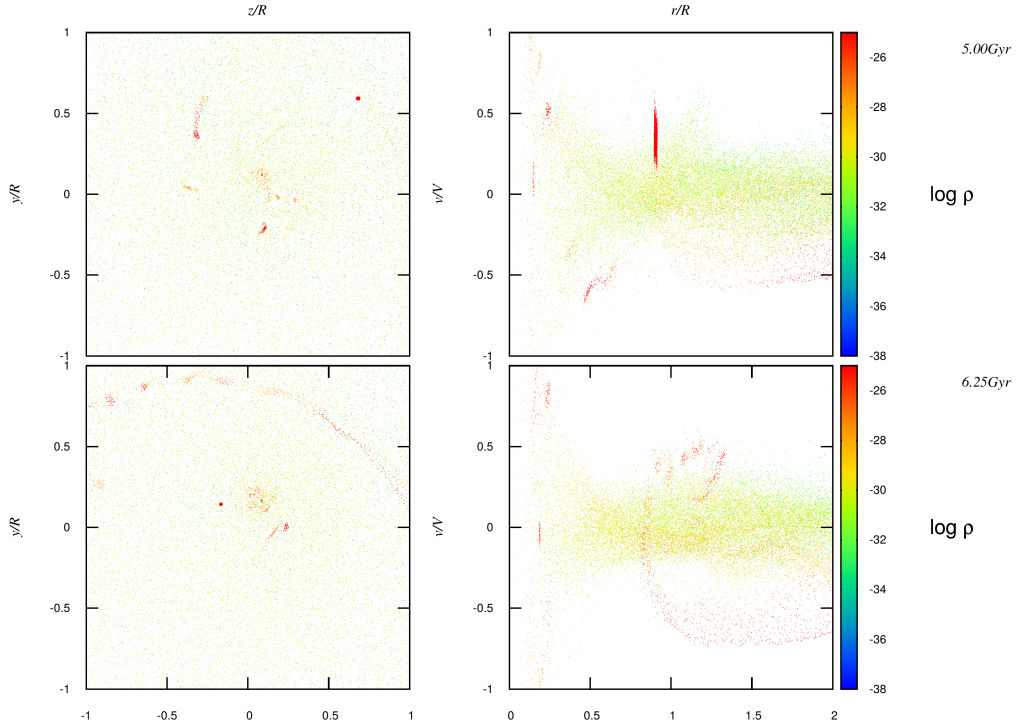

Figure 4.8: *Left Panel:* Real space projection on the $z-y$ mapped with density. *Right Panel:* Phase space projection on the $r-v_r$ plane with same density color mapping. This plot is exactly figure 4.6 but zooming to the internal region near the galactic disc for HR2. ρ is in $10^{10}\mathrm{M}_{\odot}/\mathrm{Kpc}^3$.

4.2.3 Analysis and Conclusions

Once candidates where identified, we proceeded to characterize its internal and orbital dynamics. As simulation HR3 offers abundant candidate clumps and also is the most realistic simulation of the performed three, we emphasize the analysis on it. The orbital decay of the candidates are depicted in figures 4.10 (a) and (b) which show the typical spiral decay by dynamical friction of a system embedded in a dark matter halo. Both plots were constructed by estimating the components of the center of mass position relative to the center of the host halo. The first one is the magnitude of the center of mass vector while the second one are projections of the three-dimensional orbits in the xy-plane. The candidate therefore naturally tend to orbit near the galactic disc, contributing to the young subpopulation because is recently formed and the kinematics tend to be, by spiral decay, the kinematics

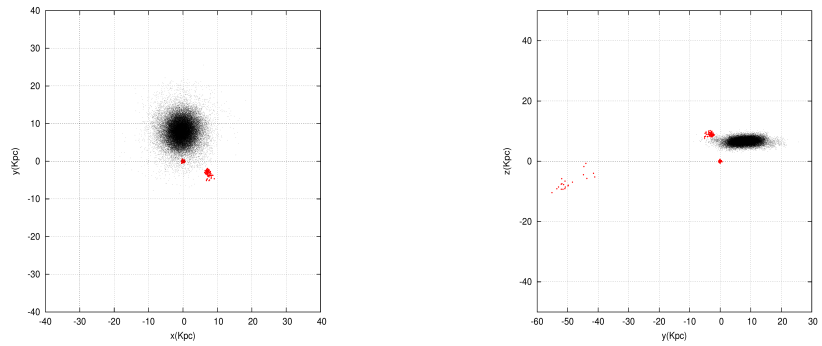

(a) (b)

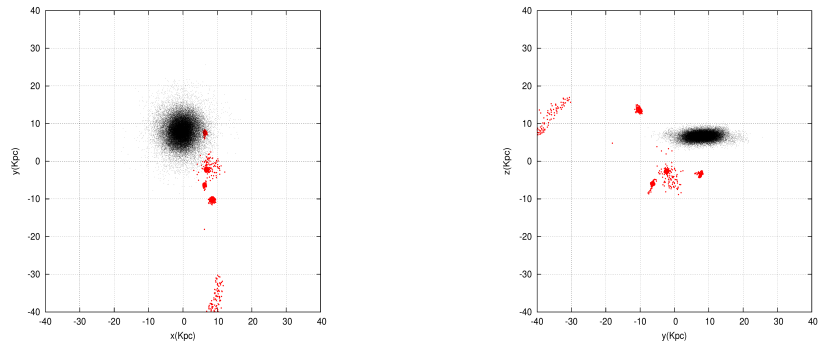

(c) (d)

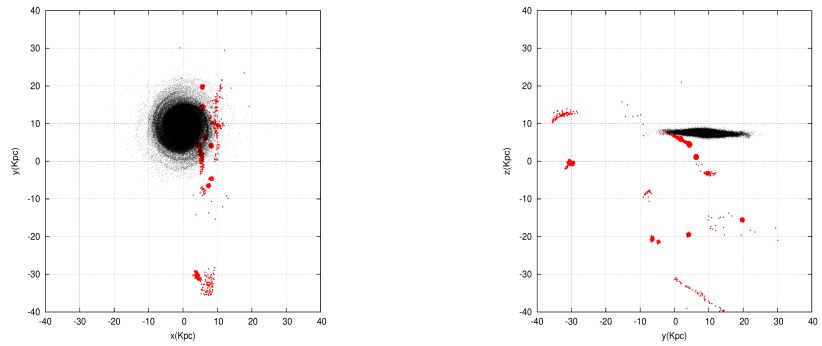

(e) (f)

Figure 4.9: Candidates identified with the algorithm described in this section. The number of clumps increase with increasing resolution. All the plots correspond to 3 Gyr simulation time. (a) Candidates in HR1 with the disc seen face on. (b) Candidates in HR1 with the disc seen edge on. (c) Candidates in HR2 with the disc seen face on. (d) Candidates in HR1 with the disc seen edge on. (e) Candidates in HR3 with the disc seen face on. (f) Candidates in HR3 with the disc seen edge on.

observed in young disc clusters. The previous conclusion is reinforced by the fact that the galactic disc has a diameter of approximately 20 Kpc comparable with the size of the orbits when the candidate had lose the majority of its orbital energy 4.10 (b). It can also be noted in subfigure (a) that the candidates appear at different epochs of the minor merger, some of them are faster disrupted and others survive several perigalacticon passages. Thus, we can argue that the candidates are stable structures in time that can survive for more than 1 Gyr as a consequence of the physical processes involved in their evolution, not just due to numerical fluctuations. Several candidates exhibit irregularities in their trajectories that could be due to multiple causes, including the stripping away of many or all of the particles with which it was identified. The evolution of the candidates follows until they are about to merge with galactic disc after several perigalacticon passages.

Subfigure 4.11 (a) shows the time evolution of of the minimun resolvable mass for each cluster according to 4.4, which remains much smaller than the local Jeans mass for the clumps depicted in figure 4.12. Thus it can be ensured that the structures obtained come from physical processes rather than numerical artifacts due to SPH fragmentation. Figures 4.11 (b), (c) and (d) shows the internal dynamical evolution of the candidates, subplot (b) shows the contraction and expansion of the outer boundaries of the clumps as a consequence of the interaction with the host galaxy. The estimation of the tidal radius for each candidate was done via equation 2.24. The values of the tidal radii are mainly greater than the observed values of the tidal radii of the globular clusters by an order of magnitude, suggesting that the clumps corresponds with the observed cores in Giant Molecular Clouds [Harris 1999]. The moments of greater contraction, that is, when the tidal radii are the smallest, occur in the passage of the candidate through the galactic disc as can be noted by the comparison of figures 4.11 (a) and 4.10 (a).

The tidal heating ΔE was estimated by the equation 2.28 by comparing the changes in velocities of the candidates due to the interaction of the galaxy. Tidal heating are prominent when the clumps are passing through the galactic disc (Figures 4.11 (c) and 4.10 (a)), moments in which the tidal radii are minimum. Disc shocks are therefore a disruptive factor rather than promote the development of compact cores via gravitational instabilities. This transfered energy to the candidate will heat the gas within it, suppressing the star formation process.

The central density 2.23 shows that innermost region of each clump exhibit a central density oscillation as can be seen in figure 4.11 (d). The central density oscillates independently of the passages through the galactic disc, evidencing that the central region of the clumps are stable structures, but its oscillations are not gravothermal ones, they are induced by the interaction with the host halo given their short life times.

Figure 4.13 shows the mass evolution of each candidate in HR3. For all the candi-

dates, the principal constituent is gas. The high picks of host dark matter content

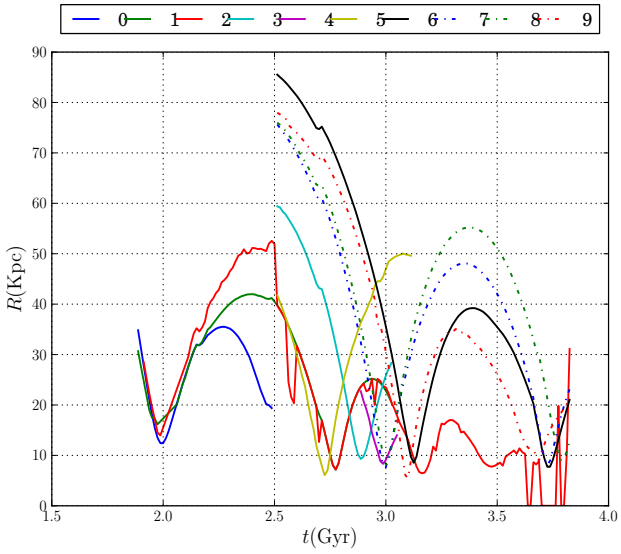

(a)

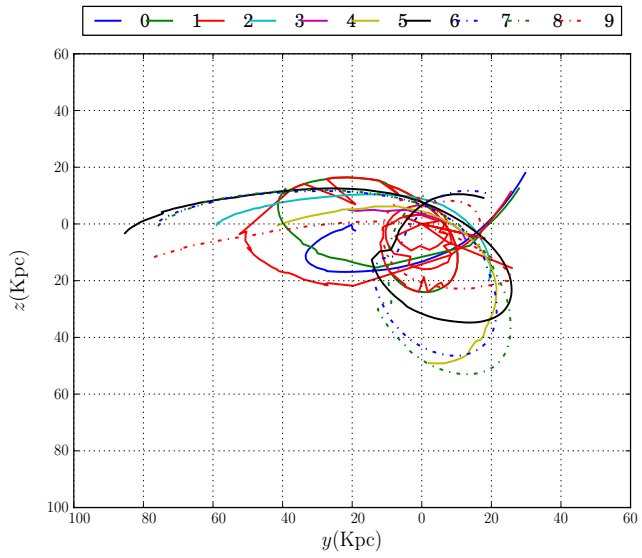

(b)

Figure 4.10: Orbit structure of the candidates identified in HR3. (a) Magnitude of the galactocentric vector position as a function of time. (b) Projection of the orbits in the yz plane.

present in the candidates are circumstantial particles that are counted by the algorithm when the candidate traverses the central region of the dark halo where the density is sufficiently high to cause the miscounting of host dark particles as candidate particles.

The candidate labeled as Candidate 0 was the only formed by gas and particles of another species. Figure 4.13 (a) clearly shows that the predominant mass component is the dark matter of the satellite from where it comes. This dark matter component is not circumstantial, and is an integral part of this candidate during its lifetime. The rest of the candidates are basically cores of gas, without dark matter or disc stars, and even more striking, no new stars formed within the candidate. Without stars, the candidate will never become a cluster, it will remain as a compact core of gas with high density.

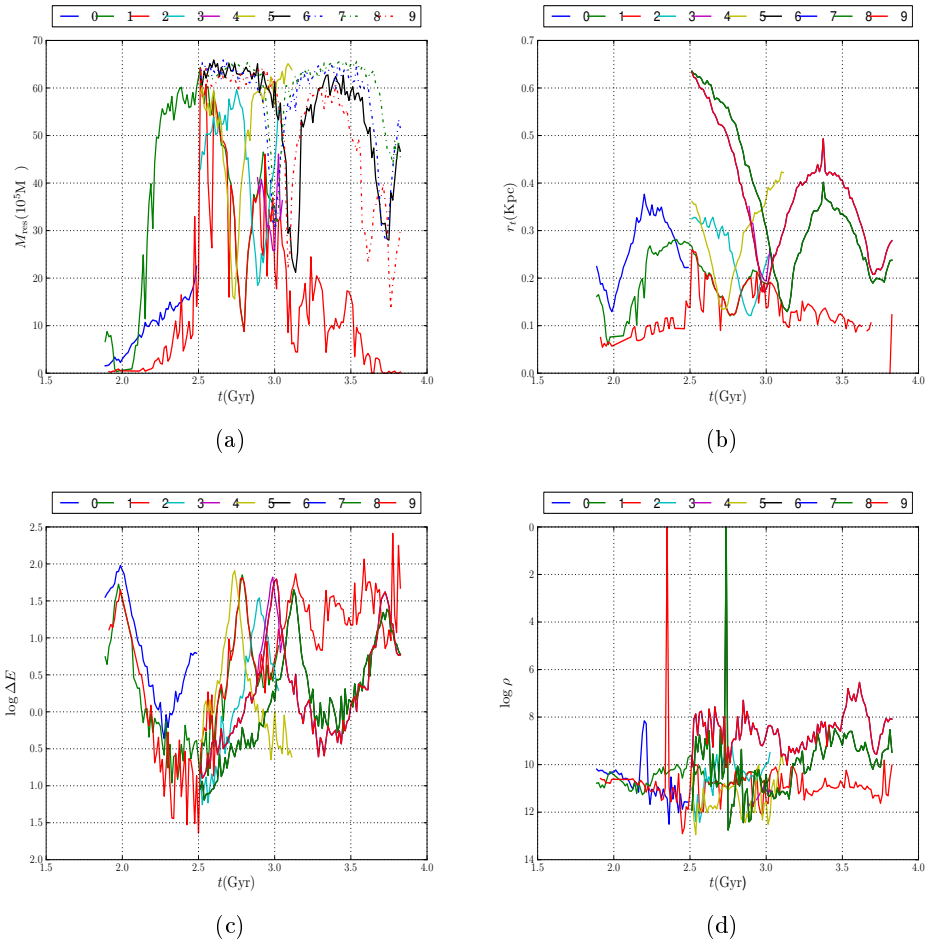

Figure 4.11: Evolution of the orbital and structural parameters in HR3. (a) Minimun resolvable mass of the candidates in time. (b) Evolution of the tidal radii of the candidates (c) Tidal heating evolution for each candidate. (d) Evolution of the central densities for each candidate.

In this simulations in particular, the lack of new stars is attributed to the isothermal gas sphere model adopted for the gas in the satellite galaxy. The temperature is so high that will inhibit the star formation in the candidates. The exploration of other

more realistic model for the distribution of temperatures in the gas is an issue that will be explored in the future.

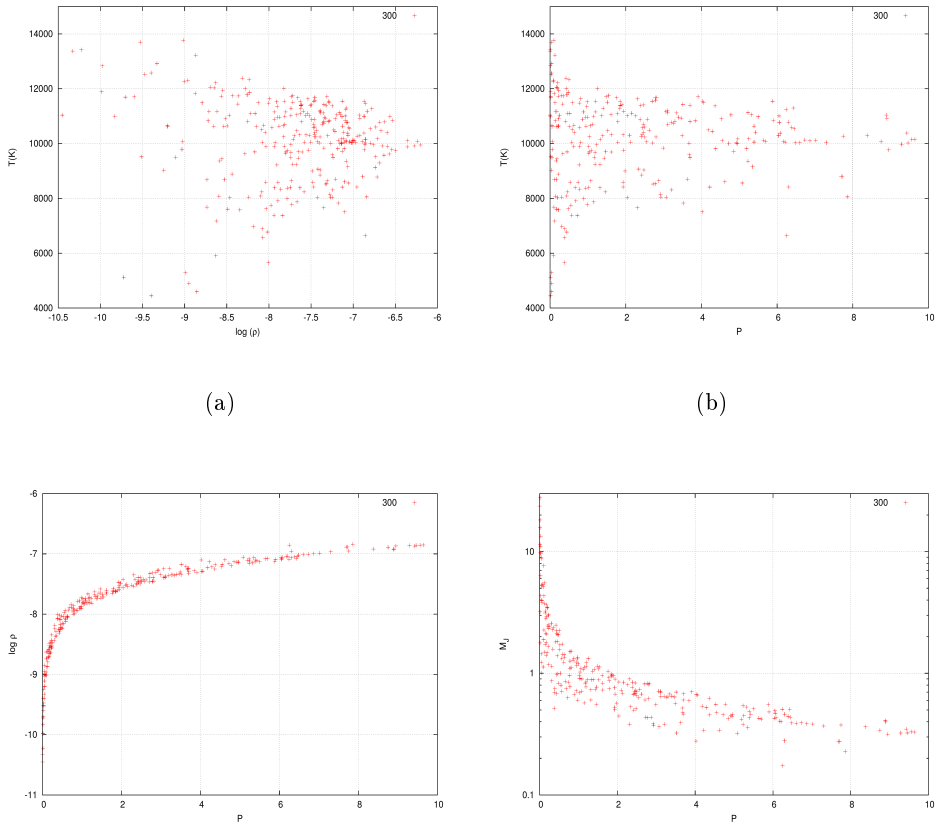

Figure 4.12: Gas thermodynamic state variables for the candidate 4 for in HR3 3.75 Gyr after simulation start at snapshot 300. (a) Temperature [K] *vs* density logarithm. (b) Temperature [K] *vs* Pressure [UnitEnergy/Kpc^3]. (c) Density logarithm *vs* Pressure [UnitEnergy/Kpc^3]. (d) Jeans mass *vs* Pressure.

However, the formation of new stars in the candidates is determined by the numerical mechanism adopted in the code to generate new stars from the gas. Thus, the cores may still satisfy the physical conditions for collapse, fragment and give birth to a stellar cluster. Figure 4.12 summarizes the thermodynamical state variables of the gas particles in the clump and their relation with the Jeans mass. While many particles are subjected to low pressure with high Jeans masses that do not lead to collapse and star formation, several other particles posses the necessary attributes to lead to star formation in the clumps.
Therefore, we can conclude that the cores formed in a tidal stream could become

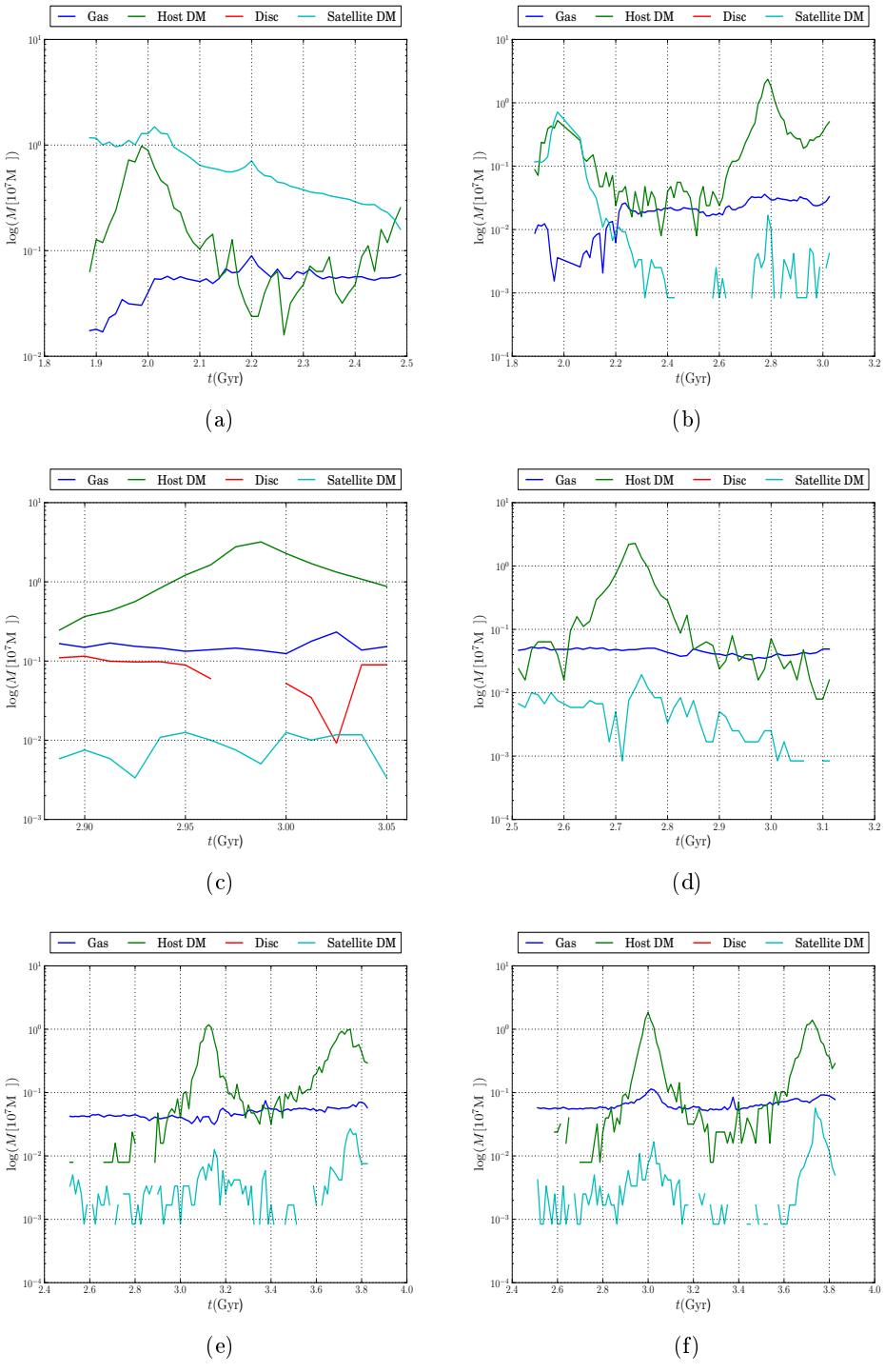

Figure 4.13: Mass as a function of time for each candidate, segregated by type. The prominent peaks in the plots are due to the pass of the cluster through the central region where the algorithm take into account particles of the dark halo that actually do not belong to the candidate (a) Candidate 0. (b) Candidate 1. (c) Candidate 4. (d) Candidate 5. (e) Candidate 6. (f) Candidate 7.

Jeans unstable in at least a region of it, thereby forming a new star system. The cores have masses of the order of $10^5 M_\odot$, the resulting stellar system would be around $10^3 M_\odot$ which is consistent with the young clusters observed in the galaxy.

Chapter 5

General Conclusions

In this work, we ran a series of N-body simulations of satellite galaxies undergoing minor mergers with a larger host galaxy, looking for globular cluster-like systems in the tidal stream formed by the tidally stripped material from the satellite. The work was divided in two main parts: The first part was performed to explore the possibility of a completely devoid of gas satellite as progenitor of the cluster-like structures while the second part was dedicated to simulations with isothermal gas in the satellite galaxy.

Then we performed several estimations in the simulations to identify the stream and the possible globular cluster candidates inside it. The two approaches adopted to identify candidates were the estimation of the gravitational potential in order to found potential wells generated by cluster-like structures and the estimation of the phase-space density which will reveal the presence of cluster-like candidates as density picks.

The analysis with the gravitational potential does not reveals any potential well apart from the potential of the satellite itself. By contrast, the density estimation clearly identifies overdensity regions in which a cluster-like structure could be formed. As a first conclusion we argue that without gas, no cluster-like candidates could be formed as none of the overdensities show a definite morphology or stability over time. When the gas was included, several cluster-like clumps appear.

Running with gas physics results are remarkably different. The candidates obtained proved real physical structures that lived for a considerable amount of time and whose orbital evolution leads them to be objects in the surroundings of the galactic disk. The total absence of stars formed within the clumps is mainly due to the thermodynamic setup of the gas as an initially isothermal sphere and probably due to the implementation/parameters of star formation we use. However, examining the thermodynamic evolution of the clump, the probability of a collapse under real physical conditions seems plausible since quantities as the pressure and the Jeans mass within the candidates could favor cluster formation.

Thus, the exploration of realistic temperatures distributions and another more realistic hydrodynamical parameters of the gas is the path to follow in order to complete the final conclusion of this work; globular clusters can be formed in tidal streams

of gas rich satellites. The validity and scope of this main conclusion should be tested by running simulations with higher resolutions with the above considerations in the physical modeling of the problem. This is the roadmap for future work that contributes to improving and supplementing the results presented here.

Bibliography

[Bate 1997] M. Bate and A. Andreas. *Resolution requirements for smoothed particle hydrodynamics calculations with self-gravity.* MNRAS, vol. 288, pages 1060–1072, 1997. (Cited on page 48.)

[Mo 1998] H. Mo and S. Mao and S. White. *The Formation of Galactic Dics.* MNRAS, vol. 295, pages 319–336, 1998. (Cited on page 24.)

[Aaerseth 2003] S. Aaerseth. *Gravitational N-body Simulations.* Cambridge University Press, First Edition, 2003. (Cited on page 33.)

[Teyssier 2002] R. Teysser. *Cosmological hydrodynamics with adaptive mesh refinement. A new high resolution code called RAMSES.* A&A, vol. 385, pages 337–364, 2002. (Not cited.)

[Springel 2005] V. Springel and T. Di Matteo and L. Hernquist. *Modelling Feedback from Stars and Black Holes in Galaxy Mergers.* MNRAS, vol. 361, pages 776–794, 2005. (Cited on pages 21 and 24.)

[Moster 2010] B. Moster *et al. Constraints on the Relationship between Stellar Mass and Halo Mass at Low and High Redshift.* ApJ, vol. 710, pages 903–923, 2010. (Cited on page 24.)

[Sanderson 2013] R. Sanderson and A. Helmi. *An Analytical Phase-Space Model for Tidal Caustics.* MNRAS, vol. 435, pages 378–399, 2013. (Not cited.)

[Gunn 1972] J. Gunn and J. Gott. *On the Infall of Matter into Clusters of Galaxies and Some Effects on their Evolution.* ApJ, vol. 176, pages 1–19, 1972. (Cited on page 18.)

[Cohn 1989] H. Cohn and P. Hut and M. Wise. *Gravothermal Oscillations after Core Collapse in Globular Cluster Evolution.*. ApJ, vol. 342, pages 814–822, 1989. (Cited on page 16.)

[Benacquista 2013] M. Benacquista and J. Downing *Relativistic Binaries in Globular Clusters.* Living Reviews in Relativity, vol. 16, pages 4–68, 2013. (Cited on pages 15 and 16.)

[Spitzer 1987] L. Spitzer. *Dynamical Evolution of Globular Clusters.* Princeton University Press, First Edition, 1987. (Cited on pages 15 and 16.)

[Kippenhahn 2012] R. Kippenhahn and A. Weigert and A. Weiss *Stellar Structure and Evolution.* Springer, Second Edition, 2012. (Cited on page 12.)

[Elmegreen 1997] G. Elmegreen and Y. Efremov. *A Universal Formation Mechanism for Open and Globular Clusters in Turbulent Gas.* ApJ, vol. 480, pages 235–245, 1997. (Cited on pages 12 and 19.)

[Chabrier 2003] G. Chabrier. *Galactic Stellar and Substellar Mass Function.* PASP, vol. 115, pages 763–795, The University of Chicago Press on Behalf of the Astronomical Society of the Pacific, 1993. (Cited on pages 12 and 13.)

[Mo 2010] H. Mo and F. van den Bosch and S. White. *Galaxy Formation and Evolution.* Cambridge University Press, Ltd., First Edition, 2010. (Cited on page 13.)

[Draine 2011] B. Draine. *Physics of the interstellar and intergalactic medium.* Princeton University Press, Ltd., First Edition, 2011. (Cited on page 12.)

[LeBlanc 2010] F. LeBlanc. *An Introduction to Stellar Astrophysics.* John Wiley and Sons, Ltd., First Edition, 2010. (Cited on page 11.)

[Sandage 1993] A. Sandage. *Temperature, Mass, and Luminosity of RR Lyrae Stars as Functions of Metallicity at the Blue Fundamental Edge. II..* AJ, vol. 106, pages 703–718, 1993. (Cited on page 11.)

[Sandage 1970] A. Sandage. *Main-Sequence Photometry, Color-Magnutide Diagrams and Ages for the Globular Clusters M3, M13, M15 and M92..* ApJ, vol. 162, pages 841–870, 1970. (Cited on pages 10 and 11.)

[Rowlett 2005] R. Rowlett *et al. How Many? A Dictionary of Units of Measurement.* University of North Carolina, 2005. (Cited on page 9.)

[Carney 1998] B. W. Carney. *Stellar Evolution in Globular Clusters.* Star Clusters, Springer, 1998. (Cited on pages 9 and 10.)

[Lightman 1978] A. Lightman and S. Shapiro. *The Dynamical Evolution of Globular Clusters.* Reviews of Modern Physics, vol. 50, pages 437–481, 1978. (Cited on pages 9, 14 and 15.)

[Durrell 1993] P. Durrell and W. Harris. *A Color-Magnitude Study of the Globular Cluster M15.* AJ, vol. 105, pages 1420–1441, 1993. (Cited on pages 8 and 10.)

[Martinez 2010] D. MartÃnez-Delgado *et al. Stellar Tidal Streams in Spiral Galaxies of the Local Volume: A Pilot Survey with Modest Aperture Telescopes.* AJ, vol. 140, pages 962–967, 2010. (Cited on pages 5 and 20.)

[Belokurov 2006] V. Belokurov. *et al.. The Field of Streams: Sagittarius and its Siblings.* ApJ, vol. 642, pages 137–140, 2006. (Cited on pages 5 and 20.)

[Bekki 2003] K. Bekki. and K. Freeman. *Formation of ω from Ancient Nucleated Dwarf Galaxy in the Young Galactic Disc.* MNRAS, vol. 346, pages L11–L15, 2003. (Cited on page 19.)

[Bekki 2002] K. Bekki. and M. Chiba. *Formation of Galactic Disk Globular Clusters in Early Dissipative Minor Merger.* ApJ, vol. 566, pages 245–251, 2002. (Cited on pages 5 and 18.)

[Harris 1998] W. E. Harris. *Globular Clusters Systems.* Star Clusters, Springer, 1998. (Cited on pages 5, 6, 8 and 10.)

[Zepf 1993] S. Zepf. and K. Ashman. *Globular Cluster Systems formed in Galaxy Mergers.* MNRAS, vol. 264, pages 611–618, 1993. (Cited on page 5.)

[Li 2004] Y. Li and M. Law and R. Klessen. *Formation of Globular Clusters in Galaxy Mergers.* ApJ, vol. 614, pages L29–L32, 2004. (Cited on page 5.)

[Ashman 1992] K. Ashman and S. Zepf. *The Formation of Globular Clusters in Merging and Interacting Galaxies.* ApJ, vol. 384, pages 50–61, 1992. (Cited on pages 5 and 18.)

[Peebles 1968] P. J. E. Peebles and R. H. Dicke *Origin of the globular star clusters.* ApJ, vol. 154, pages 891–908, 1968. (Cited on pages 4 and 5.)

[Cezario 2013] E. Cezario *et al. Full spectral fitting of Milky Way and M31 globular clusters: ages and metallicities.* A&A, vol. 549, pages A60–12pp, 2013. (Cited on page 4.)

[Forbes 2010] D. Forbes, and T. Bridges. *Accreted versus in situ Milky Way globular clusters.* MNRAS, vol. 404, pages 1203–1214, 2010. (Cited on pages 4 and 5.)

[Shapiro 2010] K. Shapiro, R. Genzel and N. FÃ¶rster Shreiber *Star-forming galaxies at z 2 and the formation of the metal-rich globular cluster population.* MNRAS, vol. 403, pages L36–L40, 2010. (Cited on pages 3, 6 and 19.)

[Harris 1999] W. E. Harris. *Globular Clusters Systems: Formation Models and Case Studies.* Globular Clusters: X Canary Islands Winter School of Astrophysics, Cambridge University Press, 1999. (Cited on pages 1, 2 and 54.)

[Carroll 2007] B. Carroll and D. Ostlie. *An Introduction to Modern Astrophysics.* Pearson Addison-Wesley, Second Edition, 2007. (Cited on pages 1 and 12.)

[Binney 2008] J. Binney and S. Tremaine. *Galactic Dynamics: (Second Edition) Princeton Series in Astrophysics.* Princeton University Press, Second Edition, 2008. (Cited on pages 1, 9, 17, 21 and 44.)

[Diemand 2008] J. Diemand *et al. Clumps and Streams in the Local Dark Matter Distribution.* Nature, vol. 454, pages 735–738, 2008. (Cited on page 33.)

[Gottlober 2010] S. Gottlober, Y. Hoffman and G. Yepes. *Constrained Local UniversE Simulations (CLUES).* High Performance Computing in Science and Engineering, Garching/Munich 2009, pages 309–322, 2010. (Cited on page 23.)

[Harris 1996] W. Harris. *A Catalog of Parameters for Globular Clusters in the Milky Way.* AJ, vol. 112, pages 1487–1488, 1996. (Cited on pages 2 and 3.)

[Hernquist 1993] J. Hernquist. *N-Body Realizations of Compound Galaxies.* AJSS, vol. 86, pages 389–400, 1993. (Cited on pages 24, 25 and 28.)

[Sharma 2006] S. Sharma and M. Steinmetz. *Multidimensional Density Estimation and Phase-Space Structure of Dark Matter Haloes.* MNRAS, vol. 373, pages 1293–1307, 2006. (Cited on pages 33, 37 and 38.)

[Springel 2001] V. Springel*et al.* *Populating a cluster of galaxies - I. Results at* $z = 0$. MNRAS, vol. 328, pages 726–750, 2001. (Not cited.)

[Wetzel 2011] A. Wetzel. *On the Orbits of Infalling Satellite Haloes.* MNRAS, vol. 412, pages 49–58, 2011. (Cited on pages 29 and 30.)

[Arfken 2012] G.B. Arfken*et al.* Mathematical methods for physicists. Elsevier, seven édition, 2012. (Not cited.)

[Battaglia 2005] G. Battaglia*et al.* *The Radial Velocity Dispersion Profile of the Galactic Halo: Constraining the Density Profile of the Dark Halo of the Milky Way.* MNRAS, vol. 364, pages 433–442, 2005. (Not cited.)

[Belokurov 2006] V. Belokurov*et al.* *The Field of streams: Sagittarius and its siblings.* ApJ, vol. 642, pages 137–140, 2006. (Cited on pages 5 and 20.)

[Binney 2008a] J. Binney. *Fitting Orbits to Tidal Streams.* MNRAS, vol. 386, pages 47–52, 2008. (Not cited.)

[Binney 2008b] J. Binney and S. Tremaine. Galactic dynamics. Princeton Series in Astrophysics. Princeton University Press, second édition, 2008. (Not cited.)

[Connors 2006] T. Connors, D. Kawata and B. K. Gibson. *N Body Simulations of the Magellanic Stream.* MNRAS, vol. 371, pages 108–120, 2006. (Not cited.)

[Eggen 1971] O.J. Eggen. *The Arcturus Group.* PASP, vol. 83, pages 271–285, 1971. (Cited on page 20.)

[Eyre 2011] A. Eyre. *On The Dynamics of Tidal Streams in the Milky Way Galaxy.* PhD thesis, University of Oxford, 2011. (Not cited.)

[Fellhauer 2006] M. Fellhauer*et al.* *The Origin of the Bifurcation in the Sagittarius Stream.* ApJ, vol. 651, pages 167–173, 2006. (Not cited.)

[Fellhauer 2007] M. Fellhauer*et al.* *Is Ursa Major the Progenitor of the Orphan Stream?* MNRAS, vol. 375, pages 1171–1179, 2007. (Not cited.)

[Gnedin 1999] O. Gnedin, L. Hernquist and J. Ostriker. *Tidal Shocking by Extended Mass Distributions.* ApJ, vol. 514, pages 109–118, 1999. (Not cited.)

[Gorsky 2005] K.M. Gorsky*et al.* *HEALPix: A Framework for High Resolution Discretization and Fast Analysis of Data Distributed on the Sphere.* ApJ, vol. 622, pages 759–771, 2005. (Not cited.)

[Grillmair 2006a] C. J. Grillmair. *Substructure in Tidal Streams: Tributaries in the Anticenter Stream.* ApJ, vol. 651, pages 29–32, 2006. (Not cited.)

[Grillmair 2006b] C.J. Grillmair and O. Dionatos. *Detection of a 63 degrees Cold Stellar Stream in the Sloan Digital Sky Survey.* ApJ, vol. 643, pages 17–20, 2006. (Not cited.)

[Grillmair 2009] C.J. Grillmair. *Four New Stellar Debris Streams in the Galactic Halo.* ApJ, vol. 693, pages 1118–1127, 2009. (Not cited.)

[Helmi 1999] A. Helmi*et al.* *Debris Stream in the Solar Neighbourhood as Relicts from the Formation of the Milky Way.* Nature, vol. 402, pages 53–55, 1999. (Not cited.)

[Helmi 2004] A. Helmi. *Is the Dark Halo of our Galaxy Spherical?* MNRAS, vol. 351, pages 643–648, 2004. (Not cited.)

[Ibata 1995] R. Ibata, G. Gilmore and M. Irwin. *Sagittarius: the nearest dwarf galaxy.* MNRAS, vol. 277, pages 781–800, 1995. (Not cited.)

[Ibata 1997] R. Ibata*et al.* *The Kinematics, Orbit and Survival of the Sagittarious Dwarf Spheroidal Galaxy.* AJ, vol. 113, pages 634–656, 1997. (Not cited.)

[Ibata 2001a] R. Ibata*et al.* *A Giant Stream of metal-rich Stars inn the Halo of the Galaxy M31.* Nature, vol. 412, pages 49–52, 2001. (Not cited.)

[Ibata 2001b] R. Ibata*et al.* *Great Circle Tidal Streams: Evidence for a Nearly Spherical Massive Dark Halo around the Milky Way.* ApJ, vol. 551, pages 294–311, 2001. (Not cited.)

[Ibata 2007] R. Ibata and B. Gibson. *The Ghosts of Galaxies Past.* Scientific American, vol. 296, pages 40–45, 2007. (Not cited.)

[Johnston 2005] K. V. Johnston, D. R. Law and S.R. Majewski. *A Two Micron All Sky Survey of the Sagittarius Dwarf Galaxy. III. Constraints on the Flattening of the Galactic Halo.* ApJ, vol. 619, pages 800–806, 2005. (Not cited.)

[Kepley 2007] A.A. Kepley*et al.* *Halo Star Streams in the Solar Neighborhood.* AJ, vol. 134, pages 1579–1595, 2007. (Not cited.)

[Koposov 2010] S. E. Koposov, H.-W. Rix and D. W. Hogg. *Constraining the Milky Way Potential With a Six-Dimensional Phase-Space Map of the GD-1 Stellar Stream.* ApJ, vol. 712, pages 260–273, 2010. (Not cited.)

[Lin 1982] D.N.C. Lin and D. Lynden-Bell. *On the Proper Motion of the Magellanic Clouds and the Halo Mass of our Galaxy.* MNRAS, vol. 198, pages 707–721, 1982. (Not cited.)

[Longair 2008] M. Longair. Galaxy formation. Springer, second édition, 2008. (Not cited.)

[Majewski 2003] S. R. Majewski*et al.* *A Two Micron All Sky Survey View of the Sagittarius Dwarf Galaxy. I. Morphology of the Sagittarius Core and Tidal Arms.* ApJ, vol. 599, pages 1082–1115, 2003. (Not cited.)

[Martin 2010] N. Martin and S. Jin. *The Hercules Satellite: A Stellar Stream in the Milky Way Halo?* ApJ, vol. 721, pages 1333–1339, 2010. (Not cited.)

[MartÃnez-Delgado 2004] D. MartÃnez-Delgado*et al.* *Tracing out the Nothern Tidal Stream of the Sagittarius Dwarf Spheroidal Galaxy.* ApJ, vol. 601, pages 242–259, 2004. (Not cited.)

[MartÃnez-Delgado 2007] D. MartÃnez-Delgado*et al.* *The Virgo Stellar Overdensity: Mapping the Infall of the Sagittarius Tidal Stream onto the Milky Way Disk.* ApJ, vol. 660, pages 1264–1272, 2007. (Not cited.)

[Martinez-Delgado 2010] D. Martinez-Delgado*et al.* *Stellar Tidal Streams in Spiral Galaxies of the Local Volume: A Pilot Survey with Modest Aperture Telescopes.* AJ, vol. 140, pages 962–967, 2010. (Cited on pages 5 and 20.)

[Martinez 2010] C.A. Martinez. Estudio del origen y evolucion de la galaxia sagitario mediante simulaciones numericas de n-cuerpos. Master's thesis, Universidad Nacional de Colombia, 2010. (Not cited.)

[Mastropietro 2005] C. Mastropietro*et al.* *The gravitational and hydrodynamical interaction between the Large Magellanic Cloud and the Galaxy.* MNRAS, vol. 363, pages 509–520, 2005. (Cited on page 28.)

[Mathewson 1974] D.S. Mathewson, N.M. Cleary and J.D. Murray. *The Magellanic Stream.* ApJ, vol. 190, pages 291–296, 1974. (Not cited.)

[Mieske 2012] S. Mieske, M. Hilker and I. Misgeld. *The Specific Frecuencies of Ultra-Compact Dwarf Galaxies.* A&A, vol. 537, page A3, 2012. (Not cited.)

[Mo 2010] H. Mo, F. van den Bosch and S. White. Galaxy formation and evolution. Cambridge University Press, first édition, 2010. (Cited on page 13.)

[Munoz 2010] R.R. Muboz, M. Geha and Beth Willman. *Turning the Tides on the Ultra-Faint Dwarf Spheroidals Galaxies: Coma Berenices and Ursa Major II.* AJ, vol. 140, pages 138–151, 2010. (Not cited.)

encodingInBib